Grasping the world of research

Through the eyes of scientists

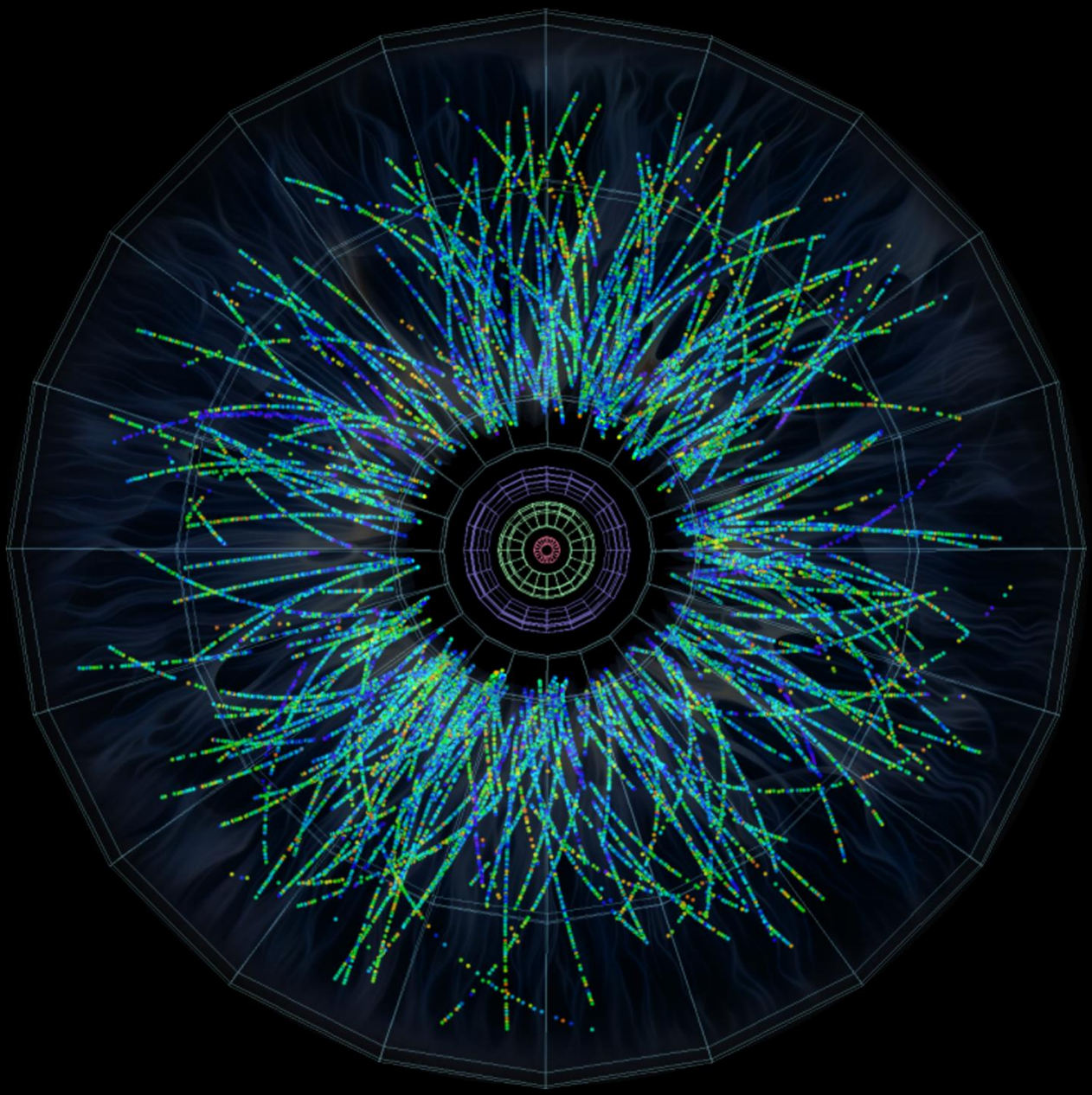

IFIN-HH

Summer student program
2017

HPD

Grasping the world of research

Through the eyes of scientists

http://niham.nipne.ro

Printed in Magurele

Table of contents

TRD Analysis

Karalius Liudas[1,2] and Ouatu Iustin[1,3]

[1] *IFIN-HH, Hadron Physics Department*
[2] *University of Birmingham*
[3] *University of Oxford*

Abstract

We investigate the behaviour of a Transition Radiation Detector (TRD) prototype in high counting rate environment. Such conditions are created using a collimated radioactive ^{55}Fe source, a tunable X-Ray tube and a laser as radiation sources. We also use pulser signal to test the Data Acquisition (DAQ) system. We observed that the free running DAQ, operating the TRD prototype, starts exhibiting saturation at signal rates of 75 kHz/channel and limitations appear at rates above 150 kHz/channel. Nevertheless there are time windows in the DAQ operations which can accommodate rates up to 700 kHz/channel which may be used to access particle rates on the TRD even above the design limit of 10^5 $particles/cm^2$. Such particle rate capabilities of the TRD prototype are still under scrutiny.

1 Introduction

Hadronic Physics Department has embarked to deliver completely reliable transition radiation detectors (TRD's) for the Compressed Barionic Matter(CBM) experiment at FAIR(Facility for Anti-proton and Ion Research), at GSI(Gesellschaft fur SchwerIonenforschung), in Darmstadt, Germany. At GSI one studies highly compressed nuclear matter created in relativistic heavy-ion collisions aiming to analyze in detail the Quantum Chromo-Dynamics (QCD) phase diagram. The CBM experiment is a fixed-target experiment and it includes several layers of detectors [1]. In particular, the role of the TRD's is to discriminate between electrons and pions and to serve as tracking detector for charged particles. The detector has to have pion rejection capability-pion suppression factor of 10-20 (@90% e-efficiency), good space point resolution(around 300μm), very short collection times (below 0.3 μs) and pad granularity optimized for required tracking capabilities and data rates. In order to fully characterize the TRD's behavior under CBM conditions, the response of such detectors is currently undertaken in high counting rates environment in the HPD department of IFIN-HH where we have done our internship.

This report presents the results obtained when the detector is irradiated with radiation which mimic the high counting rate environment. The generic experimental setup consists of: the TRD prototype along with a tunable X-ray Tube, a pulser generator, a complex laser system and a collimated radioactive ^{55}Fe source as radiation sources. For a particular set of measurements a combination of such sources was used. The X-Ray tube acts as the main tool for simulating high counting rate environment while the rest of the sources were used to quantify the detector/FEE/DAQ performances during and/or after irradiation.

2 Theoretical considerations about the physical processes involved

Transition radiation(TR) is emitted when a charged particle passes the boundary of two media with different dielectric constant. Its existence was predicted in 1946 by Ginbzburg and Frank [2] . The emitted radiation is the homogeneous difference between the two inhomogeneous solutions of the Maxwell's equations of $\vec{E}$ and $\vec{B}$ in each medium separately. However, it was not studied experimentally for many years because the number of expected quanta was small [3].
The first observation of the Transition Radiation in the optical region was made by P.Goldsmith and J.V.Jelley in 1959 [4], but it has severely limited usage because of its low intensity [5] [6].

G.M. Garibian [7] showed that for ultrarelativistic charged particles ($\gamma > 1000$), where $\gamma = \frac{1}{\sqrt{(1-\beta^2)}}$ the TR should also appear in the X-ray domain. Moreover, the total energy loss should be proportional to γ. As for any form of radiation given by relativistic particles, it has a peak in the forwards direction at an angle approximately equal to $\frac{1}{\gamma}$. This results in a difficulty to distinguish between charged particles and radiation itself.

Because of the nature of the radiation itself the number of X-ray photons which appear when passing an interface of different media is proportional to the fine structure constant $\alpha = \frac{1}{137}$, so more layers of materials are needed. The space between them has to be proportional to the wavelength of the radiation. Thus, for short X-rays we need less material space than for long optical TR. As a result, we can pack more layers of material in a given volume when analyzing X-ray TR than optical TR.

The TRD consists of two parts : a radiator and a multi-wire proportional chamber(MWPC). TR X-ray photons are produced in the radiator. Charged particles enter the radiator, which is a multi-layered volume especially designed such that those particles create Transition Radiation while passing the boundaries. As an example, for a $\gamma = 2000$ factor, just 0.8 TR X-ray photons are produced, so we use more layers of radiator material.

Any particle has to have a momentum larger than a certain value in order to produce TR. In the particular case of electrons more than 1 GeV/c is needed, in comparison with pions : 280 GeV/c. This means that for a given value of the momentum, electrons have a higher probability to produce transition radiation than pions. Generally speaking, one can find information about momentum by curving the trajectory of the charged moving particles using a magnetic field.

The concept of Multi Wire Proportional Chamber (MWPC) was invented by G.Charpak et al. in 1968 [8] and has proven to have a wide impact on nuclear and particle physics in general and on detectors architecture in particular. This is due to the parallel planes of independent wires : they are under high-voltage and they all work as individual proportional counters. Using this technique we achieve high counting rates, reasonable energy, time and position resolutions with a relative cheap setup. The active gas inside the multiwire proportional chamber is ionized by the charged particles crossing it. Apart from the specific energy loss dE/dX of the particles in gas, that probability of producing TR in the radiator better helps discriminate between electrons and pions.

The detection is based on the gas inside the TRD. It is a mixture of two elements carefully chosen such that they enhance ionization and absorb unwanted radiation. The X photon from the radiator (see above) interacts with the the active gas by extracting an

electron from the gas via photoelectric effect. In this process the electrons from the inner shells of the gas are extracted, leaving the ion in an excited state. The ion de-excites via two processes :Auger electron emission and fluorescence with branching ratio of 88 % and 12 % respectively. Since the fluorescence photon will dissipate position information in the detector special care is taken to annihilate it so that it does not produce further avalanches by ionizing the gas. We used CO_2 as *quencher*. Since the probability of the photoelectric effect is proportional to Z^4, where Z is the atomic number of gas elements, we mix noble gases (Xe or Ar) along with that quencher. In our particular case, a mix of 80% Ar and 20 % CO_2 is used. Finally, the concentration of the O_2 inside the gas has to be really low (<100 ppm) to avoid energy dissipation via collisions with oxygen molecules.

Since the detection chamber is under high voltage with the drift plane set at $D : -800V$, the cathode at $C : 0V$ and the anode plane at $A : 2400V$ the free electrons drift in the electric field towards the anode wires. Close to these, the radial electrical field becomes strong enough to accelerate the electron above the gas ionizing potential and thus to produce a Townsend avalanche. The phenomenon of Townsend discharge is used in any type of gaseous radiation detectors: in particular in the TRD it helps to amplify the electric signal of the ionization electrons. The charge is spatially confined along the anode wire and thus can be used via a capacitive coupled pad read-out to estimate the spatial position of the discharge.

2.1 Experimental Set-up

The generic experimental setup consists of: TRD prototype under High-Voltage along with a tunable X-Ray Tube, Pulser, Laser and a collimated radioactive ^{55}Fe source as radiation sources. For a particular set of measurements a combination of radiation sources is used. However, X-Rays act as a main tool for simulating the high counting rate environment. Pulser of tunable frequency is also used to test DAQ system by injecting a formatted signal directly on the TRD anode wires. To test the TRD at high counting rates, the X-Ray Tube's parameters are varied, i.e. current and accelerating potential.

2.2 Front End Electronics and Data Acquisition System

Apart from the TRD chamber itself, the system consists also of the Front End Electronics (FEE) based on FASP-02 (Fast Analog Signal Processing) [9] and the FASPRO (Fast Analog Signal Processing Read Out) [10] DAQ (Data AcQuisition) also developed by the HPD team for the same purpose, in prototyping phase. In particular the FASPRO board also hosts commercial Analog to Digital Converters (ADC). The high frequency signal measured on the pads is amplified and formatted in the FASP ASIC by a two fold integration with Gaussian kernels of appropriate shaping time in order to give the signal a Gaussian like shape. The peak of such signal is then detected and held constant, forming a flat top, for a fixed time of 400 ns dictated by the 16 clock cycles needed by the ADC to digitize the signal. The DAQ runs at 40 MHz. The moment of the peak and its amplitude are thus recorded providing information on the charge deposit amplitude and time profile used to discriminate incoming particles. A picture of the flat top and the corresponding signals can be seen in figure 1.

Data format for each read-out channel-pad consists of 64 bits (channel number: 8 bits; signal: 12 bits, time: 44 bits @ 40 MHz clock frequency) and is stored in individual

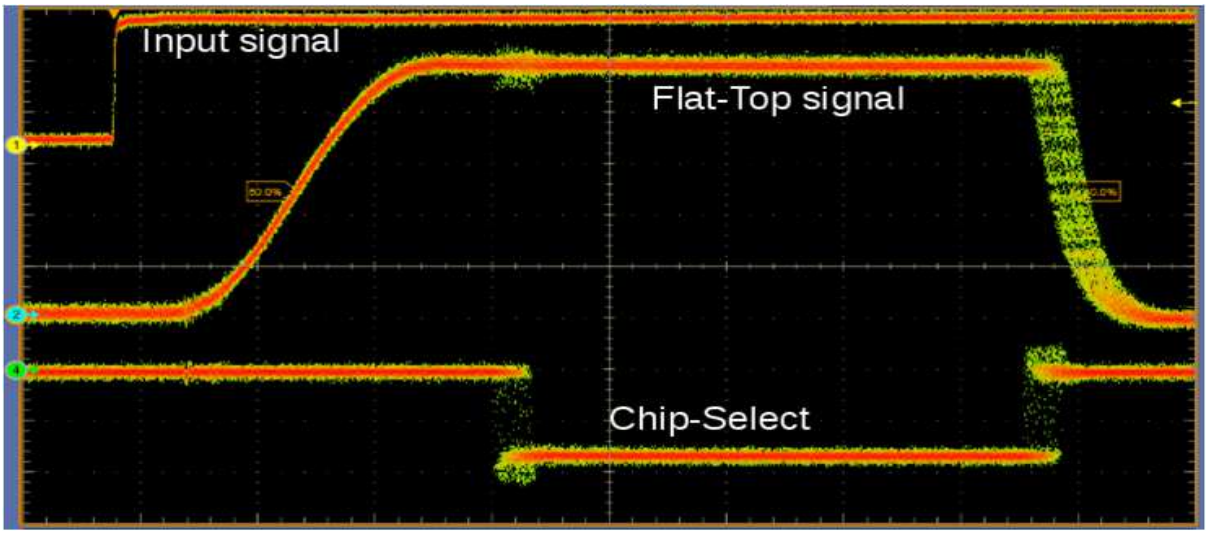

Figure 1: The flat top signal produced by FEE. Chip select region corresponds to 400 ns as mentioned. The time span of the rising and dropping part of the flat top are ASIC constants not depending on the signal amplitude.

buffers for each channel. These buffers allow 512 sets of such entries to be stored at a time. In case the buffer is full, new incoming data is ignored and lost without loosing further synchronicity which is re-established when the read-out pipe is cleared. The data buffers are cleared using a programmable FPGA which continuously writes them over the network to a storage drive. Both accumulation points in the read-out chain have a certain bandwidth which have to be tuned with the data rate expected from the detector. Raw data is later processed offline to account for individual particles and detailed physics observables.

3 Results

The main investigation is the estimation of the TRD event rate with respect to the the actual photon incidence rate it is exposed to. We present in figure 2 the time evolution of a set of measurements in which an increasing counting rate was simulated by varying the intensity of the X-ray tube in steps of 5μA from 5 to 100 μA and by 10μA from 100 to 110μA while keeping the accelerating voltage constant..

It can be seen from the figure that the anode current, which is used as a macroscopic measure of the amount of charge produced in the detector and thus particle rate, has a continuous increase with the X-ray tube intensity while the TRD event rate show different plateau like structures at approximately 30, 40 and 50 kHz/cm^2. Spikes of rate are also seen in the TRD measurements which reach above the mentioned plateau up to approximately 75 kHz/cm^2. In order to further investigate such behavior the following representation is useful.

In figure 3 we present the TRD signal rate calculated as the number of triggered channels in a fixed time window against the anode current. Anode current is a good measure of the rates to which the TRD is exposed, as it is independent of the FASPRO DAQ. We have used time windows of 0.5, 1, and 10 ms in order to capture different features of the process.

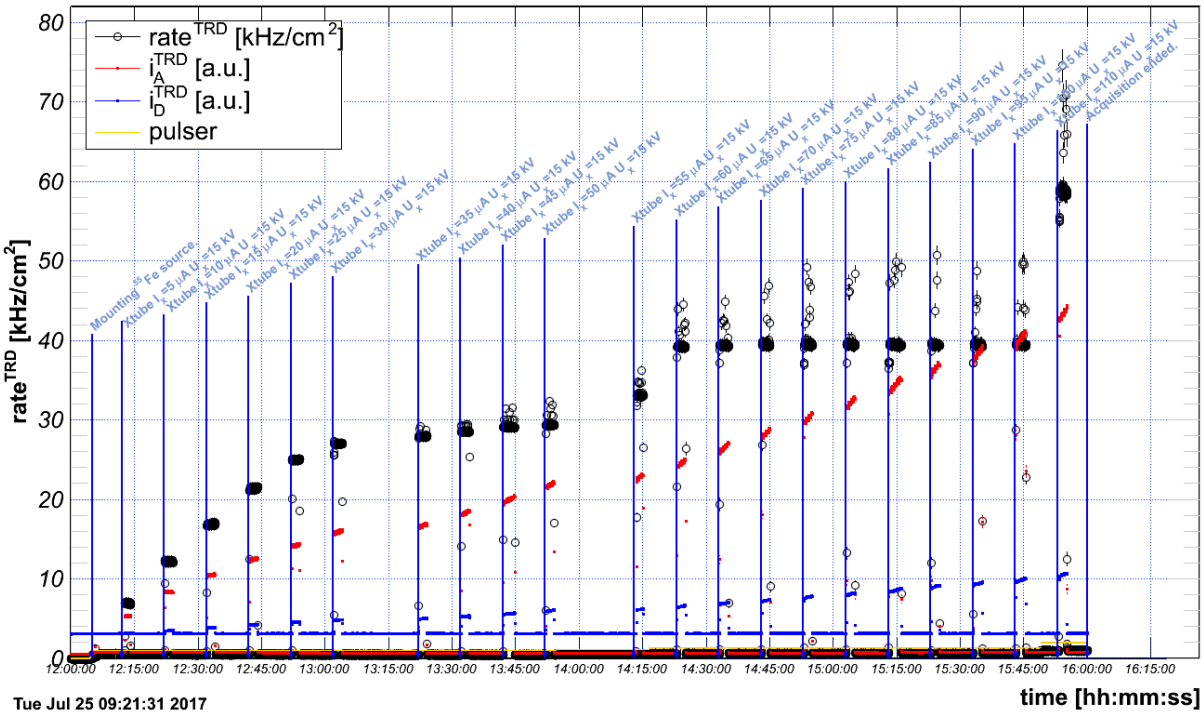

Figure 2: Different event rates are obtained with the TRD prototype (black) by varying the current of the X-ray tube. Anode (red) and drift (blue) currents are also added to the picture. Details of the experiment are added on the figure (see blue arrows). Data taken on 21.07.2017.

All three representations show an inflection point at around anode currents of $I_A \sim 8000$ of a flat rate of $R_{signal} \sim 75kHz/channel$ which indicates a saturation of the DAQ system and a branch which is further linearly increasing with I_A. The saturation can be explained by loosing events in the read-out chain in high rates environment. This is believed to be caused by insufficient bandwidths of data flow in and out of FPGA (2.2) which in turn cause individual channel's buffer clogging and data loss. However, for certain time windows DAQ delivers data at a higher rate as can be seen as the less dense scatter branch following the linear trend in figure 3. There is a second inflection point where the higher rate signals depart from the linear trend with respect to the anode current as indicated by the red line being above the measured points. Such observation may point to an actual saturation of the signal itself in the detector but a firm conclusion can not be drawn on such observable since the actual time spans of full running DAQ are essentially arbitrarily juxtaposed with the rate estimation windows.

By comparing rate plots for different time windows (figure 3), one can easily see that with increasing time window span, a smaller spread of rate values is observed. This is a statistical effect - increased time window encapsulates more triggered channels and the distribution of rates narrows down to more precise values. Thus, larger time windows are better in observing the phenomenon and in our case conclusions should be drawn from the graph corresponding to time window width of 10 ms. Hence, from figure 3 (10 ms window), we can conclude that DAQ signal rate starts saturating at 150 kHz/channel.

Investigating DAQ behavior using pulser signals, we have found a time region of full DAQ performance at a frequency of 700 kHz/channel (or, equivalently 700 kHz/cm^2). This is the peak performance of the DAQ that we have observed so far which is almost a

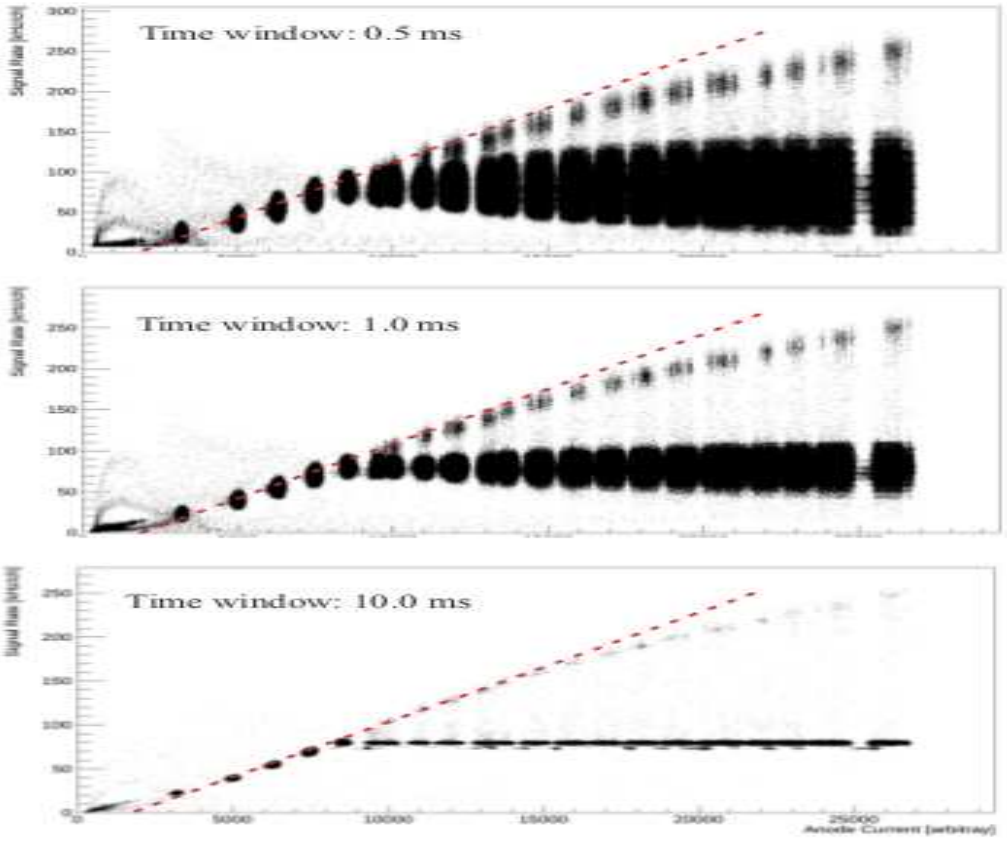

Figure 3: Scatter plots of signal rates as a function of the anode current for different time windows. One can recognize individual "scatter clouds" as peaks in figure 2. Note, red lines are drawn by hand for eye guidance purposes. Data from 21.07.2017.

factor 5 larger than that observed with random signals (figure 3) but still a factor 2 less than the theoretical capabilities of the FASP itself of approx. 1.4 MHz (from the total dead time of signal processing - see figure 1). Existence of this time window suggests that the present DAQ system, besides its actual limitations, may be used further for testing the actual rate capabilities of the TRD prototype itself but a careful study of the state of the DAQ (sending data or being blocked) has to be accurately used in the data analysis. A second version of the FASPRO data format is already available which should decrease drastically the data volume and thus allowing for operating large time spans of acquisition.

4 Conclusions and further investigations

After a careful investigation of the TRD prototype and the free running DAQ system used to read it, we have observed a signal rate saturation at about 75 kHz/channel. Limitations of the DAQ system under high counting rates were identified at 150 kHz/channel by observing departures from the linear correlation with the anode wire currents. However, for regular rate signals as produced by a pulser generator, rates up to 700 kHz/channel were observed in a selected short time window of 125 ns (figure 4) which suggests that the present DAQ can be still used successfully for measuring average particle rates of

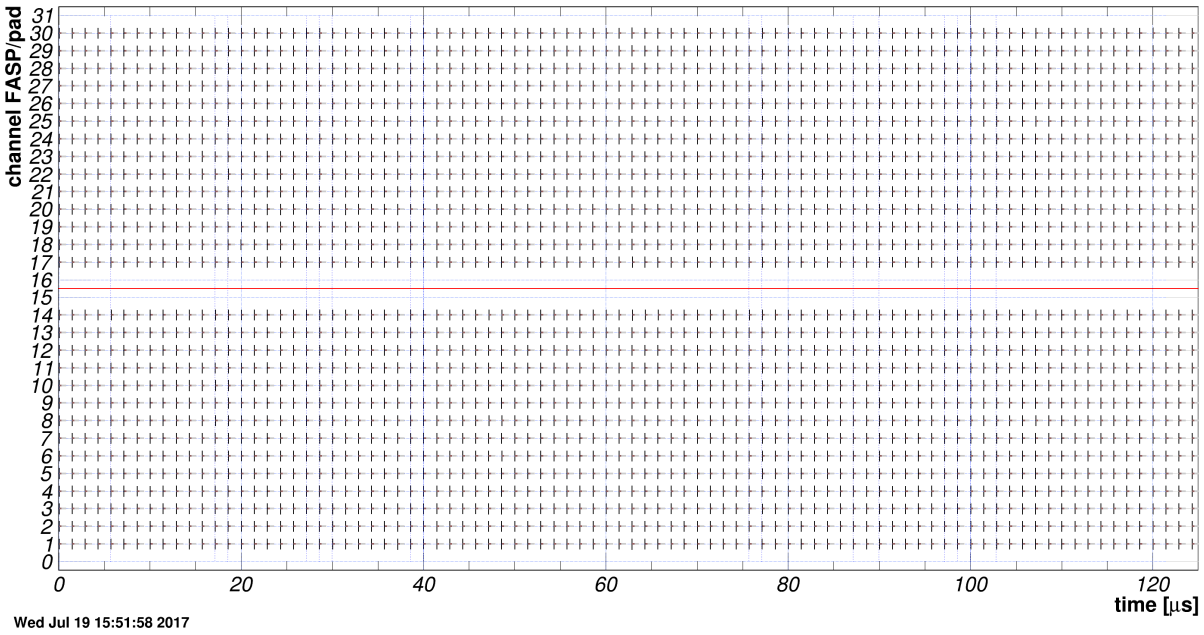

Figure 4: Testing DAQ performance with 700 kHz pulser signals injected on the anode wires. The figure shows all 32 channels in acquisition sending signals (boxes in the figure) without loss for 125 μs. Data from 14.07.2017.

10^5 $particles/cm^2$, the design limit imposed by the CBM experiment for the TRD.

5 Acknowledgements

We would like to say thank you to Prof.Dr.Petrovici Mihai for providing us with opportunity (and trusting us) to work in a competitive research department in the area of Particle Physics. To Dr.Schiaua Claudiu, for efforts and successes in helping the investigation at most crucial moments. And in particular, to our coordinator, Dr. Bercuci Alexandru, who has guided us to understanding both the goals and approaches to reach them, sharing insights and, of course, patience.

References

[1] The CBM Collacoration. Compressed Baryonic Matter Experiment. *Technical Status Report*, 2005.

[2] V. L. Ginzburg, I. M. Frank. *Zh. Eksp. Teor. Fiz.*, 16:15–28, 1946.

[3] B. Dolgoshein. *Nucl. Instrum. Meth.*, A 362:434–469, 1993.

[4] P. Goldsmith and J. V. Jelley. *The Philosophical Magazine: A Journal of Theoretical Experimental and Applied Physics*, 4(43):836–844, 1959.

[5] J. Doostens et al.,. *Phys. Rev. Lett.*, 19:541, 1967.

[6] S. Prunster et al., . *Phys. Rev. Lett.*, 18 B:47, 1968.

[7] G.M.Garibian. *Zh.Eksp.Teor.Fiz.*, 37:527, 1959.

[8] G.Charpak et al., . *Nucl. Instrum. Meth.*, 62:262, 1968.

[9] V. Catanescu et al., . *CBM Progress Report*, 2014:82, 2015.

[10] A. Bercuci et al., . *CBM Progress Report*, 2016:114, 2017.

Cosmic ray test of a high counting rate RPC prototype

Manafu Tanase-Marius[1, 2]

[1]IFIN-HH, Hadron Physics Department
[2]University of Birmingham

Abstract

During the internship at HPD, the efficiency of a high counting rate RPC prototype equipped with a front-end electronics based on NINO chip, developed by the ALICE-TOF Collaboration, was investigated. The activity started with the experimental setup mounting, readout electronic chain setting and detector conditioning. During data taking different high voltages, electronics thresholds and gas mixtures were used. A C++ software was developed for data analysis based on ROOT packages. The measured efficiency was of 93.3%, most probable being limited by an unefficient electronic channel seen in the hit distribution on the strips. A dependence on the environmental operation parameters, i.e temperature, pressure was also noticed in the data files. The time resolution of the reference plastic scintillators obtained from a Gaussian fit showed a time resolution of 105 ps for a plastic scintillator, without slewing corrections.

1 Introduction

The QCD phase diagram represents an important new area of research in the field of high-energy physics. At high temperatures and almost zero net-baryon densities, the conditions of the early Universe could be reached in the laboratory experiments using hadron collisions at ultrarelativistic energies, while at moderate temperature and high net-baryon densities states of strongly interacting matter expected to be characteristic for the core of neutron stars are anticipated to be produced at FAIR.

The Compressed Baryonic Matter [1] experiment is a fixed target experiment at the future experimental Facility for Antiproton and Ion Research, with the mission to investigate the strongly interacting matter in nucleus-nucleus collisions in an energy range between 2 and 14A GeV at SIS100 accelerator.

The experimental setup at SIS100/FAIR contains successive layers of subdetectors, with specific functions in the experiment. One of these is the TOF (*Time of Flight*) subsystem, based on MRPCs (*Multigap Resistive Plate Counter*) [2] with Multi-Strip readout architecture (MSMGRPC) [3]. The prototypes which are being designed, built and tested in Hadron Physics Department (HPD) at IFIN-HH are dedicated to the most demanding zone of the TOF subsystem in terms of counting rate and hit multiplicity, the region of low polar angles.

For the in-house and in-beam tests of these prototypes developed by HPD group, two front-end electronics (FEE) were used: NINO developed within ALICE-TOF Collaboration at CERN [4] and PADI [5] developed within CBM-TOF Collaboration. Over

the years, these prototypes were tested at COSY-Jülich and CERN-PS with minimum ionizing particles [6] and at GSI SIS-18 [7] and CERN-SPS facilities with reaction products, in a triggered mode operation DAQ system. Very good performances in terms of system time resolution of 70-80 ps and efficiencies larger than 95% [8] were obtained in these beam tests. In the last in-beam test performed at CERN-SPS in 2016, for the first time, it was used a readout system based PADI amplifier as FEE and a trigger-less mode operation DAQ system as CBM system will be operated.

The work reviewed in this paper was dedicated to the estimation of the efficiency in a cosmic - ray test performed in the Detector Laboratory of HPD, using NINO based FEE for a further comparison with the same results which are going to be obtained with PADI FEE, processing the signals delivered by the same MSMGRPC prototype.

2 Overview of the MSMGRPC constructive details

The MSMGRPC prototype based on which this work was done is considered as basic architecture for the low polar angles of CBM-TOF modules. Its structure is shown in Fig. 1.

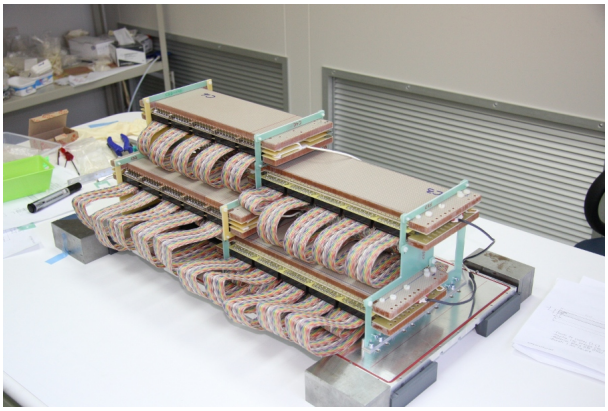

Figure 1: Photo of the MSMGRPCs mounted in a staggered disposal.

This basic architecture comprises four identical MSMGRPCs disposed in a staggered arrangement in order to assure a continuous coverage of the active area for the incident particles. Each of them has a double stack structure with multiple plan parallel layers, as can be seen in Fig. 2 and described below.

The most outer layers with a honeycomb structure, hold mechanically all the layers together. On both sides, under the honeycomb layers there are the cathode readout electrodes, separated by isolator layers from the negative polarity high voltage (HV) electrodes which are in contact with the outermost glass electrodes. They are followed by other five glass electrodes, equally spaced at 140 μm (the thickness of the fishing line used as spacer), one relative to the other. The innermost glass plates are in contact with the high voltage electrodes for the positive polarity. The positive HV electrodes are also separated by isolator layers by the anode readout electrode, positioned in the middle of the structure. Both HV and readout electrodes have a strip structure with a 7.2 mm pitch and 5.6 mm width. The glass is referred to as low resistivity (10^{10} $\Omega\times$cm) due to the fact that, in present running experiment with not so tight counting rate requirements, the resistive electrodes are made of normal float glass with a resistivity of the order of

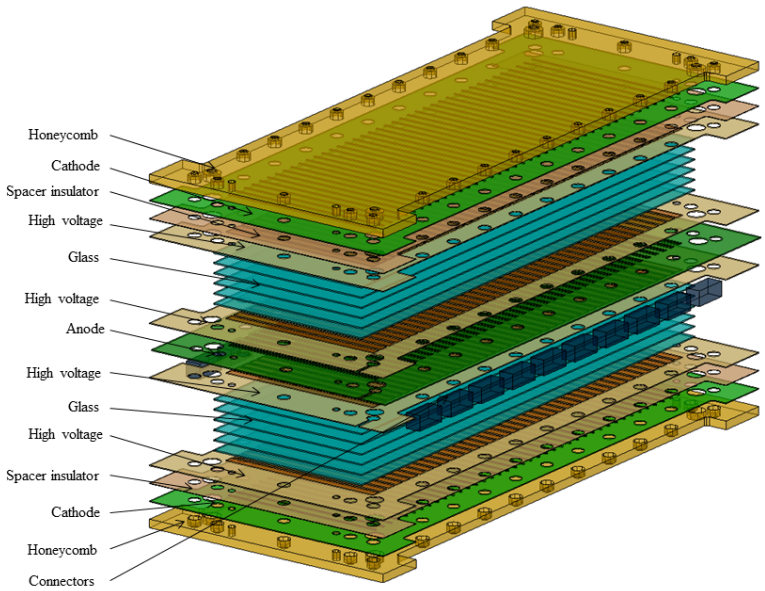

Figure 2: The multi layer structure of the MSMGRPC

10^{12} $\Omega\times$cm. The counter has 40 strips, defining an active area of 40 x 7.2 mm = 288 mm length and 96 mm width (defined by the corresponding strip length).

2.1 Experimental setup

2.1.1 Mechanical structure

I was invloved in this activity starting with the mounting of the mechanical support, installing the detectors (RPC box and plasic scintillators coupled with photomultipliers), as can be seen in Fig. 3. The two plastic scintillators were identical, having a length of 8 cm and a squre transversal cross-section of 1 cm x 1 cm. I was involved also in the equipping the detector with FEE as well as its connection to the low voltage power supply and cabling of the signals from the output of the FEE to the CAEN V1290 TDC (Time to Digital Convertor). Thus, Fig. 3 shows the intermediate step of connection of the FEE, while Fig. 4 shows routing of the cables between FEE and conversion electronics.

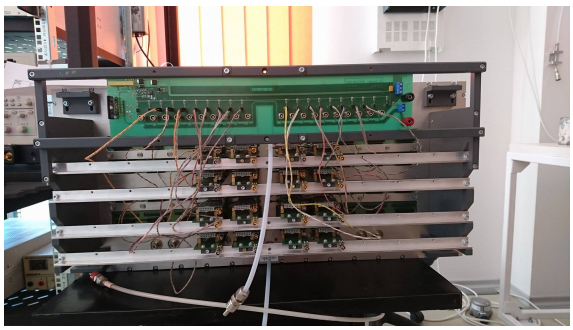

Figure 3: The RPCs box equipped with FEE, before cabling

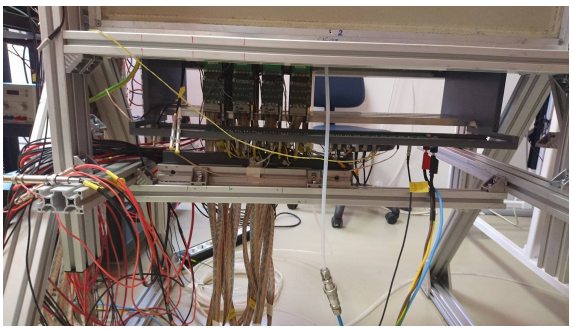

Figure 4: The RPCs box equipped with FEE - detail

The final experimental setup can be seen in Fig. 5. This image shows the two scintillators situated on top and below the RPC2012 box. Their centers were perfectly aligned with one of the four RPCs, namely (RPC3 - see Fig. 2), housed by the box in order to select only particles/trajectories which cross the active area of all three detectors, i.e. the two plastics and RPC3.

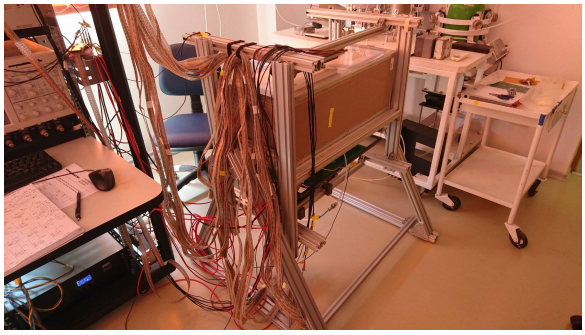

Figure 5: The experimental setup for cosmic rays test

Figure 6: Gas mixing station

A gas mixing station, showed in figure 6 provides the specific gas mixture for operation of these type of detectors. A gas mixing tank is buffering the setup. In the first part of the measurements a gas mixture based on 95%$C_2H_2F_44$ and 5%SF_6 was used. In the second part of the activity, a small percent of isobutene, i-C_4H_{10} was added. The gas mixture composition used in the last measurements was: 2.5 l/h (freon), 0.126 l/h (SF_6) & 0.125 l/h (isobutene), (90/5/5), with a total flow of 2.75 l/h .

2.1.2 Electronics

Before starting data taking, a carreful high voltage conditioning of the RPC was done. In Fig. 7 typical signals delivered by the MSMGRPC at one end of a transmission line can

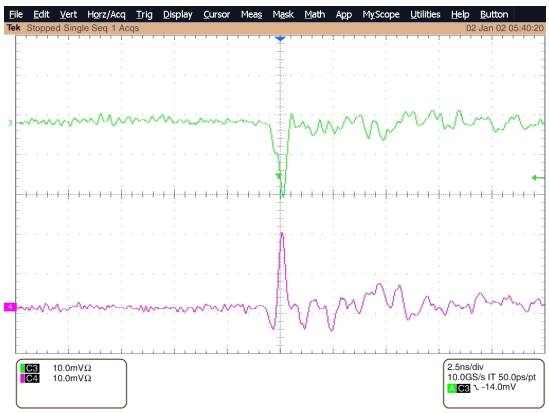

Figure 7: RPC signals at both ends of a readout channel; the anode pickup electrode's signal is green and the cathode pickup electrode's is purple

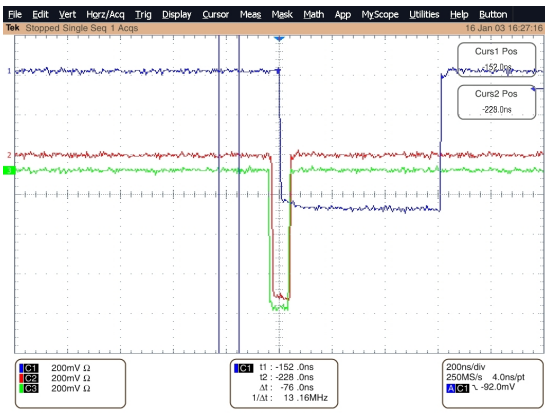

Figure 8: The green signal represents the logic coincidence between PMT1& PMT2 =C1, the red signal represents the logic coincidence between PMT3& PMT4 =C2; the blue signal represents the DAQ trigger signal C1 'OR' C2

be seen: the negative signal induced on the anode strip and the positive signal induced on

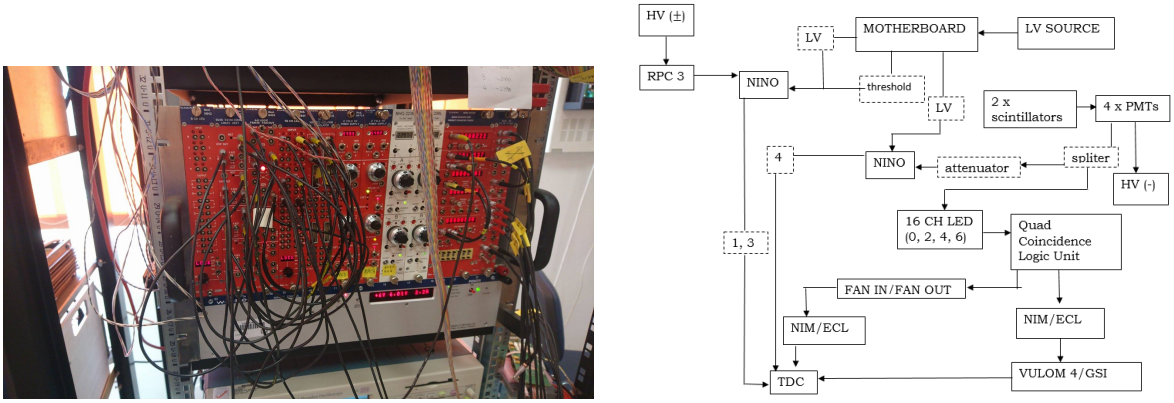

Figure 9: Left - photo of the electronics modules used to process the signals from the PMTs and NINO FEE. Right - the electronic scheme used in the measurements.

the cathode readout strips, respectively. Fig. 8 shows the coincidence of the two signals given by each pair of the photomultipliers, C1 and C2. Their logic "OR" was used as trigger signal for the Multi-Branch (MBS) data acquisition system.

A CAEN module gives the logical function 'OR' for the LVDS 'OR' RPC signals delivered by the NINO front-end cards. Their output were used in a second CAEN module which counts the number of hits in order to monitor the dark counting rate of the counter. A NIM/ECL translator was used to provide an ECL signal for CAEN TDCs synchronization, multiplied for this purpose by a FAN IN/FAN OUT module. A Quad Coincidence Logic Unit with four sections was used for setting the trigger signal. The first section does the logical condition 'AND' between signals from the first pair of PMT1 & PMT2, delivering the C1 signal, the second does 'AND' between the second pair of PMT3 & PMT4 signals, delivering the C2 signal and the third does the logical condition 'OR' between the two C1 and C2 logic signals.

In Fig. 9 - left are shown electronic modules used in the experiment and in Fig. 9 - right is presented the electronic scheme of the experiment. The four signals delivered by the PMTs were split and sent once to a leading edge discriminator in order to be used as trigger for the DAQ system as well as to an attenuator coupled with a NINO front-end card for recording their time and time over threshold information.

3 Experimental procedure

The mechanical structure involved multiple measurements in order to have a high mechanically accuracy, whilst the electronics cards were tested piece by piece, as well the PMT signals, cables connecting the electronics etc. were carrefully tested. The PMTs were operated to $\sim$ 2300 V. As it was already mentioned, the RPC HV was raised slowly, over a period of a few hours up to $\sim$ 5400 V. Through this process, the resistive electrodes reach a steady state potential and the potential microimpurities inside the detector are burned out. Thus, the dark current decreases and the quality of the data increases.

Since the data taking started, multiple files were acquired until the end of the project, corresponding to various operation conditions in the detector. To process these data the ROOT programming package and C++ language was used. A basic pilot program was developed, which was continuously updated toward a multidimensional analysis and estimation of the RPC the efficiency.

4 Results and Interpretation

The conditioning effect in terms of dark counting rate monitoring was studied on two MSMGRPCs: RPC3 and RPC4. Each measurement had a time interval of 10 s. The Fig. 10 shows this conditioning efect. In the same time the value of the dark current was recorded for each counter. The RPC3 shows a dark current less than 1 nA, which is the lower limit of which the corresponding power supply unit is measuring. The 2 - 3 nA measured for RPC4 could be the offset with which the HV power supply unit is measuring at the 5400 V applied potential. The efficiency is defined by the formula :

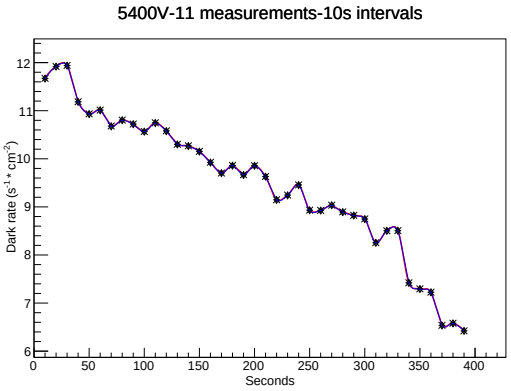

Figure 10: The decline in the number of hits in RPC in time intervals of 10s

$$\epsilon = \frac{RPC\ \&\ PMT(1\&2)\ \&\ PMT(3\&4)}{PMT(1\&2)\ \&\ PMT(3\&4)} \tag{1}$$

The numerator represents the total number of coincidences between a hit in the RPC with a hit in both scintillators corresponding to the same particle going through the 3 detectors, whilst the denuminator represents the total number of coincidences between the scintillators only.

The time it tooks the particle to travel from on scintillator to the other (at any entrance angle) is defined by the difference of the mean of the times measured at the both ends of each platic scintillator:

$$ToF_{plastic} = \frac{1}{2}(T_1 + T_2) - \frac{1}{2}(T_3 + T_4) \tag{2}$$

The incident particles can come at any angle and in any place along the scintillators.

The NINO based FEE used for amplification and discrimination of both the MSMGRPCs and plastic scintillators signals were feed in the CAEN V1290A TDCs. The leading edge (LE) of the LVDS signal provide the time information while the difference between the trailing edge (TE) and LE is proportional with the amplitude of the signal. This difference is later used in the off-line analysis for walk effect (dependence of the time information on the amplitude of the signal) corrections. In the performed analysis only signals which have a positive value for both trailing and leading edge are accepted.

The measurements started with an applied high voltage of 5400 V. In figure 11 - left the hit distributions with no condition (triggered by only one scintillator) for hits with signal in both strip ends is shown while in Fig. 11 -right, the hits distribution with coincidence between the two scintillators is presented. In the measurements 31 strips,

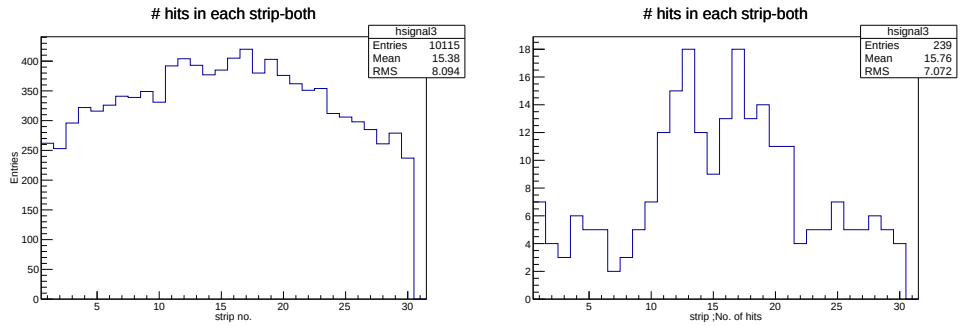

Figure 11: The hits distribution with signal in one scintillator, peaking in the middle as expected - left; the hits distribution with coincidence between the two scintillators - right.

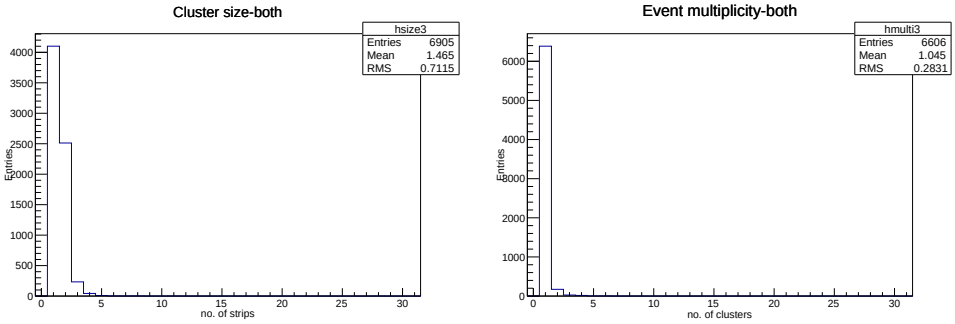

Figure 12: The cluster size distribution with a mean of ∼1.5 - left. The MSMGRPC hit multiplicity with a mean of ∼1.05 - right.

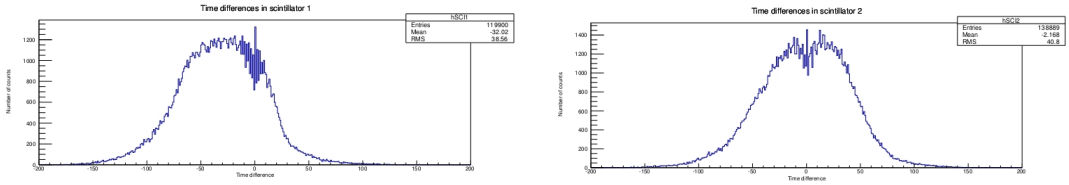

Figure 13: The position on the the top (a) and bottm (b) scintillators.

readout at both ends were used. Zooming in on the peaks in the center, a stairway-like deep was observed, especially when the background was removed by asking for coincident signals between both scintillators, as it is shown in Fig. 11. In the middle of the RPC3 there is a gradual decrease in the number of counts on the middle bins. Even it seems to be within statistical errors, due to the low coincidence statistics, this was identified as a pattern which could be due to a higher effective threshold of corresponding electronic channels .

The distribution in Fig. 11 - right, which consider only coincident hits in the three detectors (MSMGRPC and plastic scintillators) shows the observed picked structure in the middle. The number of coincidence hits between both scintillators goes to 96 particles. The number of hits for MSMGRPC end-up strips goes to 83 and at end-down to 84; at both-ends we got 83 concidences, obviously. This low statistics was obtained in about four days of continuous operation and could be explained by the small area of the scintillators together with the fact that the solid angle is very small. Using equation 1, the efficiency

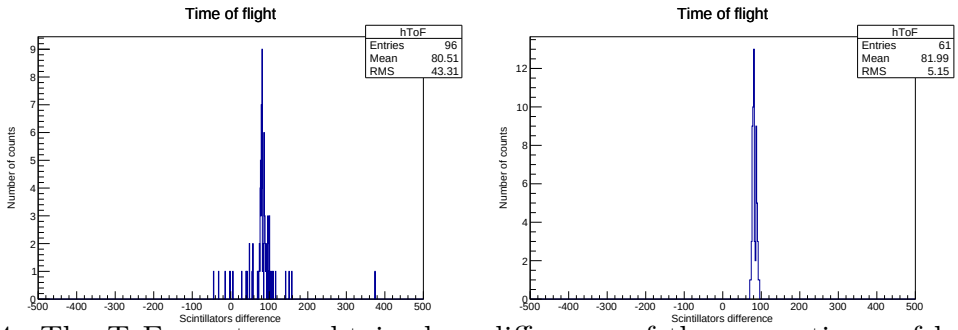

Figure 14: The ToF spectrum obtained as difference of the mean times of both plstic scintilators : left - spectrum with the full coincident statistics (1 ch./bin), right- spectrum after removing the tails (2 ch./bin).

of the RPC3 operated with NINO with this data was $\epsilon = 86.5\%$, lower than the expected value of at least 95%. A further cleaning of the background of the TOF spectrum obtained with the pladtic scintillators, increased this value to 93% as it will be shown below. In addition, more aspects were analysed, such as the cluster size and hit multiplicity seen in Fig. 12.

The cluster size represents the number of strips with signal in a single hit (when a particle goes through the RPC, the developed avalanches inside the gas gaps induce signals on more than one strip). A mean cluster size of 1.5 strips was obtained (see Fig. 12 - left) for 7.2 mm strip pitch.

The hit multiplicity represents the number of clusters per event and it had a mean of 1.04 hits per event (see Fig. 12 - right). Due to the fact that we measured cosmic muons, only in the case of showers more than one hit was identified on the active strips.

The plots in Fig. 13 show the position of the hit on each of the two scintillators. The position is obtained from the difference of the times measured at the both ends for each of them.

It can be seen that bins extend on both ranges and they are not centered on bin zero due to the uncorrected time offsets. In Fig. 14 - left the ToF spectrum obtained with the platic scintillators is shown, in a 1 channel per bin histogram. Fig. 14 - right the plot shows the ToF spectrum in a 2 channels/bin histogram with a cut in the channel range [70:95] which takes out the hits corresponding to the tails of the TOF spectrum. Removing the background hits the obtained efficiency increases to $\epsilon = 90.2\%$.

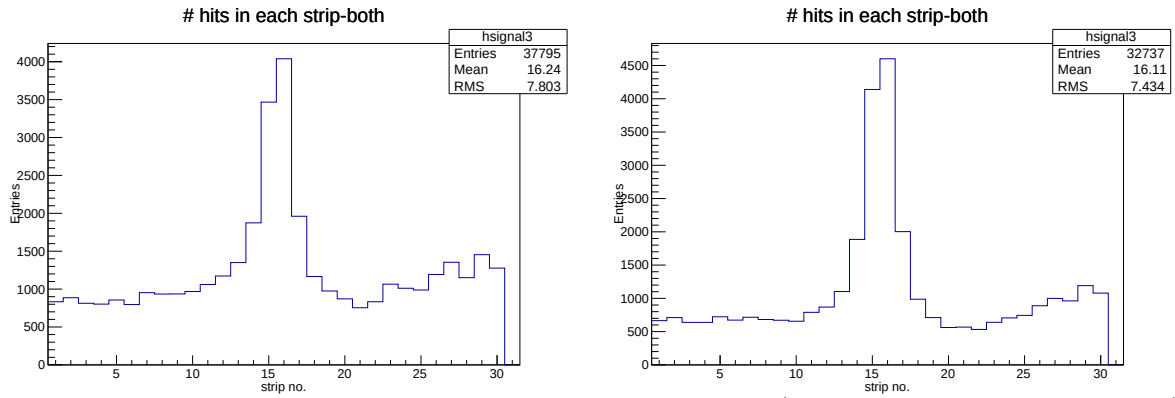

Figure 15: The hits distribution for signal at both ends (5.5 kV - left, 5.6 kV - right); they have much cleaner distributions

A new set of measurements was made raising the RPC HV to 5500 V with the same

gas mixture. The hits distribution for signal on both strip ends, triggered alternatively by each scintillator and with coincidences in both scintillators, respectivelly, can be seen in Fig. 15 - left for 5500 V applied voltage and Fig. 15 - right for 5600 V. The plots look cleaner than before, as expected with an increase in voltage. The distribution peaks in the middle of the RPC in both cases.

The cluster size and hit multiplicity have similar distributions as for the previous 2 files, with an expected small increase in the mean cluster size value.

The total number of coincidences going through both scintillators was 257. The coincident hits with plastic scintillators on up-end strips of the RPC are 205, on down-end strips are 202 and on both-ends they are 202. This gave an efficiency of $\epsilon = 78.6\%$ and with the ToF cut the efficiency went up to $\epsilon = 84.3\%$.

Although the voltage across the RPC was increased, the efficiency does not improved. In addition, a dependence on the high room temperature experienced during these measurements was noticed for the dark rate of the RPC, which may lower the efficiency.

Two more files were written for isobuthene gas mixture, with HV for the RPC at the same 5500 V, two more with 5600 V and two more with 5700 V.

The first characteristics for these sets of data was the hits distribution with coincident signals in both strip ends as seen in Fig. 16.

As it can be seen, the distribution is clean, with a middle peak. They have similar behaviours, increasing in height and peaking in the middle of the RPC. However, in the data for the RPC at 5600 V and isobuthene containing gas mixture, the structure in the hit distribution plot is again observed.

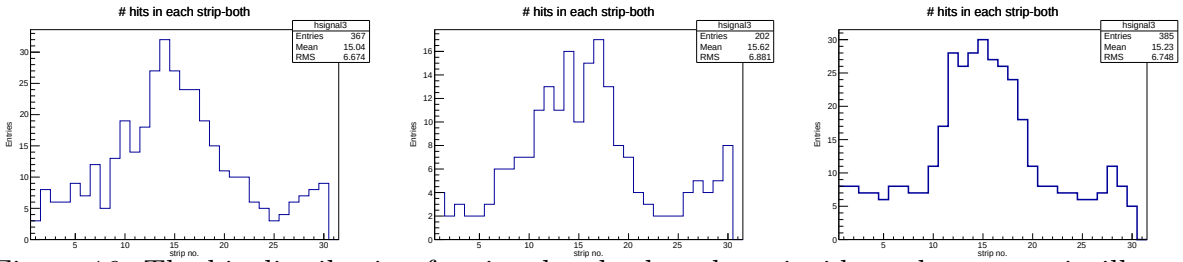

Figure 16: The hit distribution for signal at both ends -coincidence between scintillators for isobuthene files(5.5 kV left, 5.6 kV middle, 5.7 kV right)

The estimation of the cluster size as a function of the applied high voltage showed no clear relationship between the RPC voltage and the cluster size was observed.

The results obtained are summarized in Table 1. The table list the efficiecies obtained asking for coincident signals in both scintillators and with a tail cut applied in the scintillators TOF spectrum, to the data for each type of file. The efficiency took into consideration the data with signals in both strip ends of the RPC. After finishing analysing the files separately, the ones with similar setting conditions for operation of the plastic scintillators were put together for better statistics and ploted: the files with 5400V and 5500V with a 2D correlation plot of the position on the scintillators (sci1 vs. sci2) and a ToF plot of the files with 5500V, 5600V and 5700V corresponding to the period of operation with isobuthane gas mixture. The ToF spectra were fitted with a Gaussian (fig. 17 & 18). The 2D position scatter plot shows the wide range of angles through which the cosmic rays can go through the scintillators. If only a particular value of the solid angle is considered, then the plot would look like a straight line with the property 'x=y'. In addition, a value of σ is 6 channels standard deviation corresponds to a 150 ps system time resolution, if we take into consideration the 25 ps/channel calibration of the

	5500V iso files		5600V iso files		5700V iso files	
	both sci	with TOF cut	both sci	with TOF cut	both sci	with TOF cut
PMT	143	90	125	85	136	91
RPC -up	116	84	108	78	111	83
RPC -down	116	84	107	76	109	82
RPC -both	116	84	106	76	109	82
Efficiency	81.1%	93.3%	84.8%	89.4%	80.1%	90.1%

Table 1: The summary of the efficiency measurements under different operation conditions and cuts.

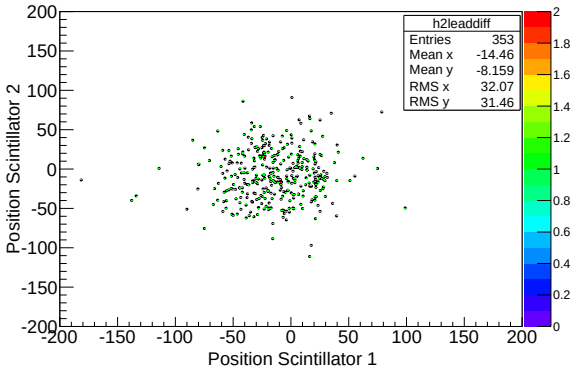

Figure 17: The 2D position correlation in scinitllators

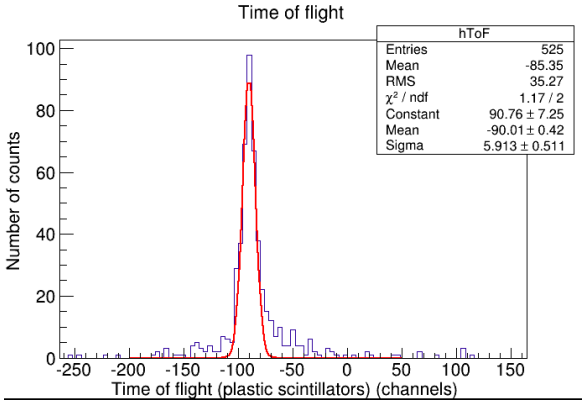

Figure 18: Plastic scintillators ToF for merged files with similar conditions; the spectrum is fitted with a Gaussian.

TDC bins. Assuming that the scintillators and photomiltipliers are identical, then the time resolution of one scintillator is obtained from the standard deviation divided by $\sqrt{2}$. Therefore, the time resolution of one scintillator is $\sigma = 105$ ps.

A pattern was noticed in the hits distribution with coincidence between two scintillators with the above discussed structure in the middle of the distribution.

More time would have been needed to investigate, analyse and identify the source of this structure. Due to time constraints and the fact that data were being proccessed for this report up to the final day, this was not possible.

5 Conclusion

This project investigated the efficiency of the MSMGRPCs operated with NINO FEE using a MBS DAQ system. The measured efficiency was of 93.3%, most probable being limited by an unefficient electronic channel seen in the hit distribution on the strips. Obviously, more investigations are needed. The plastic scintillators system time resolution yielded a sigma of 150 ps, without any correction for walk effect and postion dependence. Thus, the time resolution for one single plastic scintillator coupled with its photomultiplier was estimated to be $\sigma =$ 105 ps. A cluster size of 1.5 strips was measured. The hit multiplicity had the expected distribution for cosmic ray test. Since a different DAQ system is needed to be able to process signals from PADI FEE, after its implementation, both NINO and PADI8 FEE will be used on the same RPC in order to have a dirrect

comparison the efficiencies obtained with the two fast amplifiers with the same DAQ.

6 Acknowledgements

I would like to thank Dr. Mariana Petriş, my supervisor, for guiding me throughout this project and showing me the path on which I should go, around which I explored new things and learned so much. Also, special thanks to Prof. Dr. Mihai Petrovici for providing help and insights on work and life aspects. I would also want to thank Dr. Alexandru Bercuci for being so patient and teaching me the coding necessary in applying my ideas on the data taken. Special thanks go to Mr. Daniel Bartos as well, whose patience is much appreciated and who always showed me new aspects of the RPC in many details. Lastly, I would like to thank everyone from the Hadronic Physics Department, IFIN, for welcoming me and helping me enrich my knowledge in this summer internship.

References

[1] CBM Collaboration. *Eur. Phys. J. A*, 53:60, 2017.

[2] CBM-TOF Collaboration. *CBM-TOF Technical Design Report*, October 2014.

[3] M. Petrovici et al. *Nucl.Instr.and Meth. A*, 487:337, 2002.

[4] F. Anghinolfi et al. *Nucl.Instr.and Meth. A*, 533:183, 2004.

[5] M. Ciobanu et al. *IEEE Trans. Nucl. Sc.*, 61:1015, 2014.

[6] M.Petrovici et al. *Journal of Instrumentation Volume 7 November 2012 (JINST 7 P11003)*, 2012.

[7] M. Petriş et al. *Journal of Physics: Conference Series, Volume 533, 012009, 2014*, page 012009, 2014.

[8] M. Petriş et al. *Journal of Instrumentation, Volume 11, September 2016 (2016 JINST 11 C09009)*, 11, September 2016.

CBM time-of-flight inner wall design

Ionescu Irina Maria[1,2]

[1]IFIN-HH, Hadron Physics Department
[2]Bucharest Technical University

Abstract

During my Summer Student Program in the Hadron Physics Department of IFIN-HH I was involved in 2D and 3D modeling of the Rezistive Plate Counter (RPC) - double sided geometry - for the Compressed Baryonic Matter (CBM) experiment. Based on SolidWorks software I started also the mechanical strength simulation of the RPC modules within the CBM TOF detector system. These modules contain the RPC counters and associated electronics. The analysis was concentrated on Module 1, the most complex and the heaviest in the whole assembly, with a total estimated weight of 120 kg.

1 Introduction

The Facility for Antiproton and Ion Research (FAIR), at the GSI Helmholtz Centre for Heavy Ion Research in Darmstadt, Germany is is a new accelerator complex which will deliver high intensity beams of ions and antiprotons for experiments in the fields of nuclear, hadron, atomic and plasma physics. By a comprehensive measurement of rare probes, the CBM experiment at FAIR intends to address physics topics such as the equation-of-state of nuclear matter at densities close to that in the core of neutron stars, properties of hadrons in a dense medium and charm producion mechanism close to threshold energy and its propagation in dense nuclear matter. The two configuration of the experimental setup are shown in Fig. 1, including the Muon Chamber (MUCH) detector (left) and the Ring Imaging Cherenkov (RICH) detectors respectively [1, 2].

2 Brief History of the RPC

2.1 The Spark Counter

The first gas detector taking advantage of the improved time resolution was the Spark Counter, a gaseous avalanche detector with parallel plate geometry. It consist of a stack of metal electrodes placed in a sealed box filled with a gas (such as helium, neon). When a charged particle from a cosmic rays travels through the box, it ionizes the gas. If a high enough voltage can be applied between the electrodes before the initied ionisation disappears, sparks are produced along the trajectory of ionising particle.

2.2 Parallel Plate Avalanche Chambers

A Parallel Plate Avalanche Chamber (PPAC) is a single gap gaseous detector very similar to the Spark Counter. However, they are operated in avalanche mode; streamers and discharges are unwanted side effects in this type of detector. It normally consists of two planar electrodes made of metal, or metalized ceramic or plastic, kept apart at a fixed distance of 0.5 to 2 mm by precise spacers. Their advantages include a fast response and an increased rate capability of up to $10MHz/cm^2$. The time resolution is in the range of 100 to 250 ps.

2.3 The Resistive Plate Chamber

The RPC consists of two parallel plate electrodes (see Fig. 2). At a large gas gain a change occurs in the avalanche dynamics, then the avalanche charge carriers influence the electric field in the gas gap and hence their own propagation and multiplication (the space charge effect). If the gas gain is further increased, photons can start to contribute to the propagation of the avalanche and streamers appear. At a later stage, a conductive channel can be formed between the two electrodes, through which the local electrode surfaces are discharged [3].

In Fig. 3, a schematic image of the development of an avalanche in an RPC and the electric field deformations caused by the avalanche charges at large gain is presented. As a function of the applied electric field (E_0 in figure) the following processes are taking place:

a. Some gas atoms are ionized by the passage of a charged particle and an avalanche is ignited.

b. The avalanche size is large enough to influence the electric field in the gas gap.

c. The electrons reach the anode while the ions are drifting much slower.

d. The ions reach the cathode and the charges in the resistive layers influence the field in a small area around the position where the avalanche develops [3].

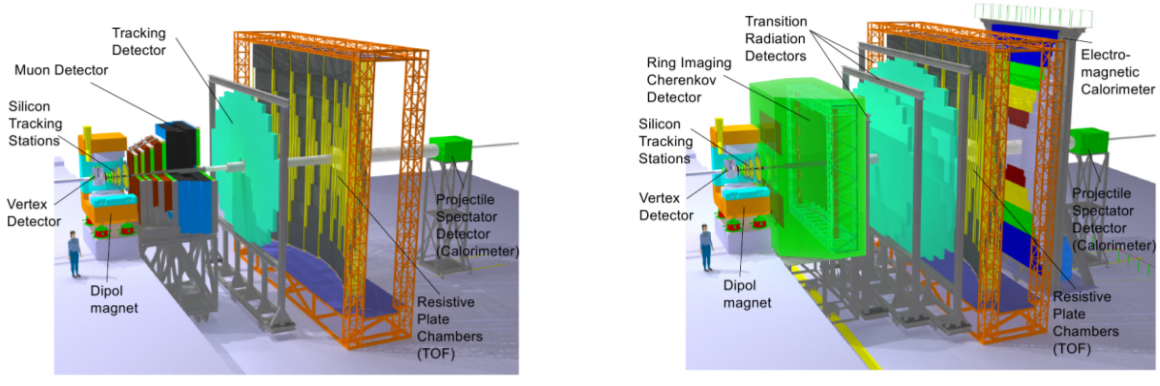

Figure 1: The CBM experiment including the MUCH detector (left) and respectively the RICH detector for electron identification (right) [1].

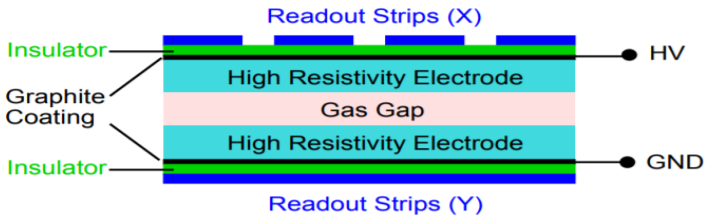

Figure 2: Schematic image of an RPC geometry [3].

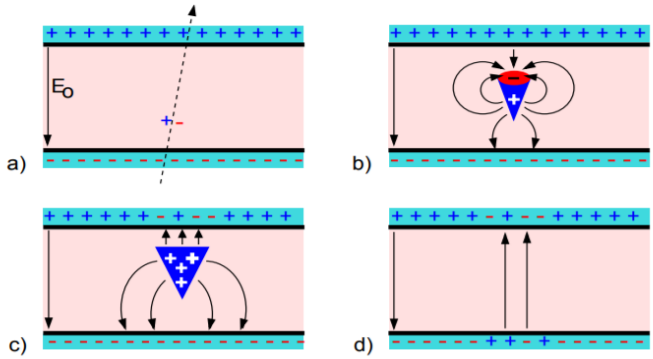

Figure 3: Schematic image of an avalanche development in the RPC [3].

3 M1 module of TOF Inner Wall

The CBM Time Of Flight (TOF) detector is used in conjunction with Silicon Tracking System (STS), RICH and the Transition Radiation Detector (TRD) for hadron (pions, kaons and protons), electrons and intermediate mass fragments identification.

The inner zone, located at the lowest polar angle, the most demanding one in terms of granularity and counting rate, is based on the strip read-out architecture, proposed and developed over the years in Hadron Physics Department [4–6].

It is under investigation the possibility to mount the TOF wall at different distances from the target position in different phases of FAIR or for different type of physics which CBM Collaboration is targeting at.

The structures of the inner zone of the CBM TOF subdetector can be followed in Fig. 4 (left) in a 3D representation for 4 different types of modules distinguished by colors. The dimensions of the inner wall (approximately $4.6m$ wide and $3m$ high) are shown in Fig. 4 (right). The inner zone wall contains 12 modules of type M1, M2, M3 and M4. Each module is build out of 3 types of RPC.

For the M1 module, 51 RPC counters are staggered in 4 layers with some overlap in order to guaranty a continuous coverage. In Fig. 5 a detailed view of the M1 module is presented as follows: 30 counters of 60 mm strip length, 18 of 100 mm strip length and respectively 3 of 200 mm length.

4 Towards mechanical strength simulation of the M1 support structure

Firstly, for a stress simulation, an overview of the materials used is necessary. The base plate and the corner fittings are made up of dural, which is a hard, but lightweight alloy of aluminum with the following mechanical properties [8]:

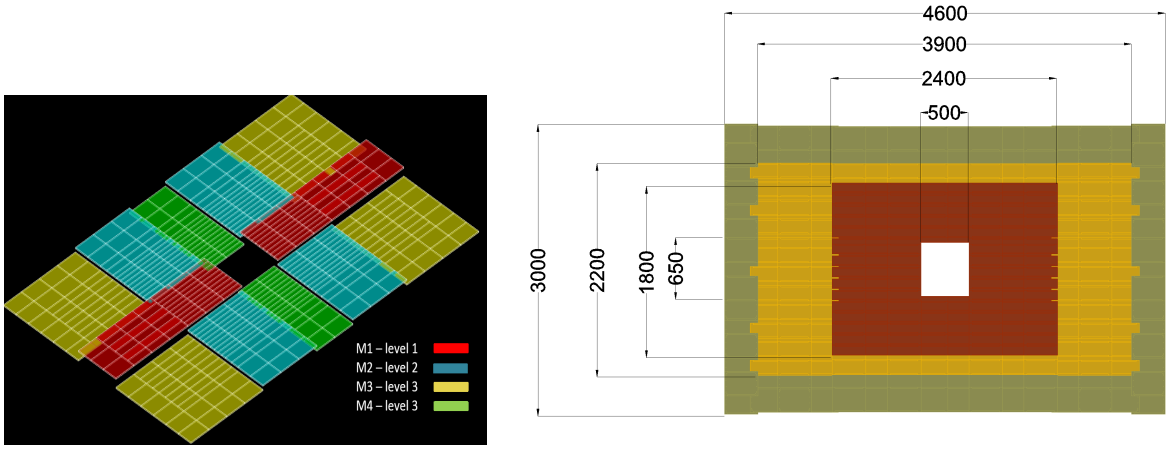

Figure 4: Modules wise structure (left) and the dimensions (right) of the CBM TOF inner zone [7]

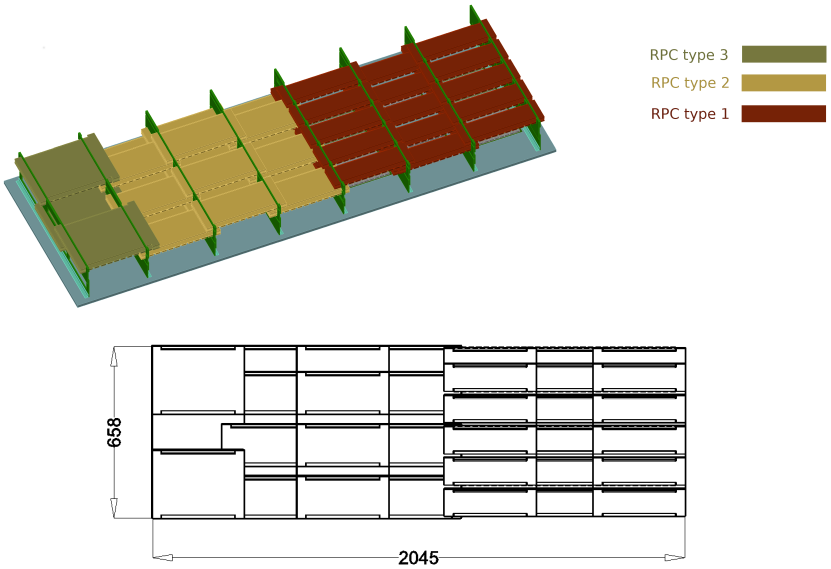

Figure 5: The 3D (top) and 2D (bottom) view of the M1 module.

Hardness (kgf/mm^2)	115-135
Modulus of elasticity (GPa)	73
Tensile strength (MPa)	420-500
Density (g/cm^3)	2.8
Izod impact strength (J/m)	8-22

The supports are made of G10(FR4), a continuous woven glass fabric laminated with an epoxy resin. This grade is extremely high in mechanical strength, has low water absorption and dissipation factors and has superior electrical characteristics, which are exhibited over a wide range of temperatures and humidities.

Rockwell Hardness M scale	110
Modulus of elasticity (GPa)	15
Tensile strength lengthwise (MPa)	275
Tensile strength crosswise (MPa)	240
Density (g/cm^3)	1.850
Izod impact strength (J/m)	5.5-7

The connection between the base plate and the "L" profile fitting is realized by 12 stainless steel M4 screw, whereas the supports are connected with nylon M5 screws, as shown in the

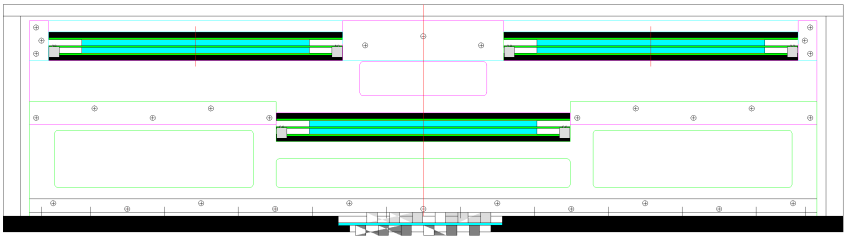

Figure 6: The 3 support types used to hold the RPC counters in the M1 module.

The RPC are kept in position by 8 support profiles which are connected to a rigid base plate. The mechanical stress orientation resulted from the counter weight is parallel to the base plate (see Fig. 7).

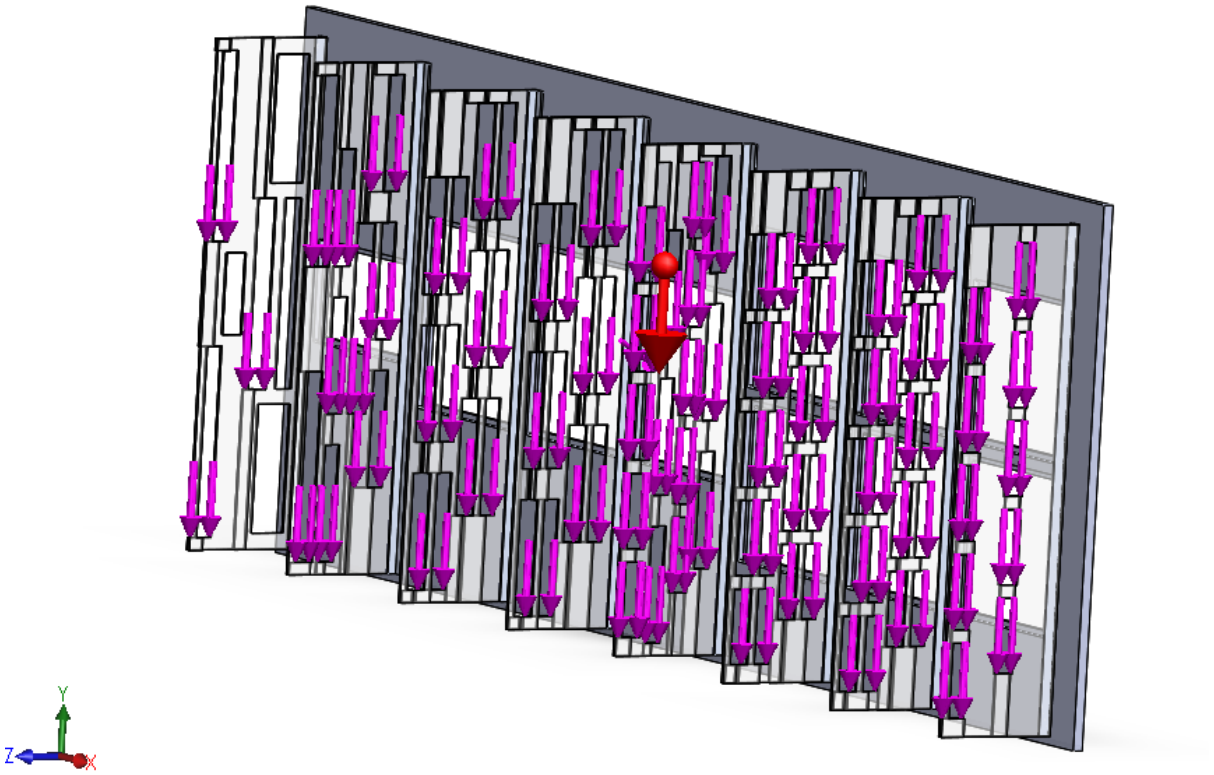

Figure 7: The load on the M1 module supports (SolidWorks).

The goal is to calculate the yield and shear stress on the supports and compare them to each resistance module for each material. For this purpose we have used the SolidWorks software. The simulation is performed in order to test the actual design. If the results are not within the accepted limits of the resistance module the mechanical design has to be re-sized and re-analyzed.

Following figures show a preliminary analysis of the support in module M1, presented as von Mises stresses (a yield criterion for complex loading conditions) (see Fig.

8 top/left), the stress along X axis (Fig. 8 top/right), along Y axis (Fig. 8 bottom/left) and the shear along the Z axis (Fig. 8 bottom/right).

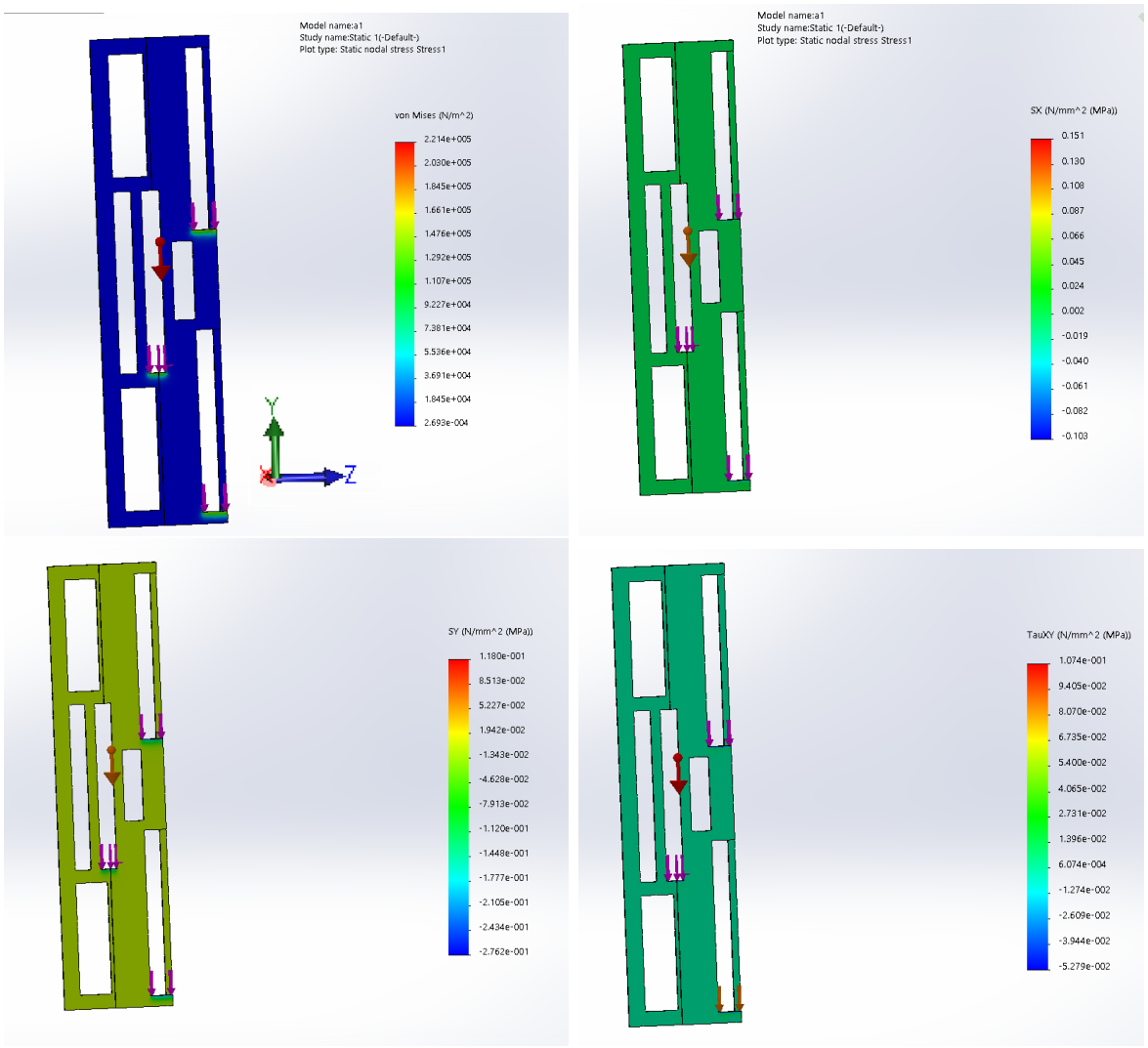

Figure 8: Stress intensity simulation : von Mises stress (top/left), X normal stress (top/right), Y normal stress (bottom/left) and shear in Z direction on XY plane (bottom/right).

5 Conclusions

The present report details the first analysis of the mechanical supports of the RPC counters from module M1 from the mechanical strength point of view. Based on SolidWorks software which was used to check if the supports are strong enough to keep the counters in position we can conclude that the current implementation is safe. The same analysis has to be done for the rest of support types of the M1 module.

During my Summer Student Internship in the HPD department of IFIN-HH I had the opportunity to work with a group involved in large international collaboration and get the flavor of the real work in the field.

References

[1] CBM Collaboration, Eur. Phys. J. A53 (2017) 60.

[2] TOF Workgroup and the CBM Collaboration *Technical Design Report for the CBM* , pp.3, 4 & 7, 2014.

[3] For a review of the PhD thesis of Christian Lippmann *Detector Physics of Resistive Plate Chambers*, pp.20-23, 2003.

[4] M. Petrovici at al., Nucl. Instr. Meth. A487 (2002) 337.

[5] M. Petrovici at al., JINST Vol 7 (2012) 11003.

[6] M. Petris at al., Journal of Physics Conf. Series 724 (2016) 012037.

[7] Laura Radulescu *Inner zone structure of CBM RPC-TOF Wall optimized for 8m distance from target, IBWAP Constanta, 2017* 2017.

[8] *http://www.acculam.com/data-chart.html*

TRD FEE analysis

Eusebiu Sutu[1,2]

[1]IFIN-HH, Hadron Physics Department
[2]University of Oxford

Abstract

During my internship, I have tested the FASP-02 chip used in the front-end electronics of the High Counting Rate Transition Radiation Detector (HCR-TRD). The chip has four functions which can be controlled. This enables the chip to be running in different working modes, which have to be tested. I have observed that in some modes the chip is not working properly so further investigation must be done by the designer of the chip itself.

1 Introduction

The Hadron Physics Department (HPD) is involved in developing HCR-TRD detectors, its associated front-end electronics (FEE) and data acquisition system (DAQ). This detector will be used in the Compressed Baryonic Matter (CBM) experiment at FAIR (Facility for Anti-proton and Ion Research), at GSI (Gesellschaft für Schwerionenforschung), in Darmstadt, Germany. For its FEE a microcircuit named FASP-02 (Fast Analog Signal Processing) was designed and for its electronic testing a test board named TB-V2 was designed.

1.1 CBM at FAIR

The experiment studies high baryion density region of the Quantum Chromo-Dynamics (QCD) phase diagram. Because of this, it is designed to be operated at extremely high reaction rates (up to 10MHz). In order to achieve this standard, there is the need of fast and radiation hard detectors, free-streaming front-end electronics and a high performance computer cluster for online event selection.[1, p.1]

1.2 HCR-TRD

The HCR-TRD is a proportional gas detector, which measures the $\gamma - dependent$ transition radiation of a particle in a stratified material. The probability of transition radiation increases with the $\gamma - factor$, which enables discrimination between particles. At CBM, the detector is used to discriminate pions and electrons. The 2D position of the particle can also be determined, due to its structure of pads. The detector has been designed to function at high counting rates, a demand set by the experiment itself.[1, p.102]

2 FASP-02

FASP-02 is the microcircuit used in the front-end electronics of the HCR-TRD designed at HPD. It has 16 spectrometric channels with corresponding trigger generators. The input polarity of the signal can be selected using the in-pol-sel function of the chip. The shape of the output analog signal can be chosen using the out-sel function as either semi-gaussian (G) or flat top (FT). The time mark at which the chip select (CS) triggering signal occurs can be selected through the tm_mk-sel function at either threshold level (THR) or at peak level of analog signal (PK/14CLK). Triggering signal can be transported to neighboring channels, the enabling of which is done using the nb-en function of the chip.[1, p.114]

2.1 Signals

The FASP-02 chip has 16 analog input (in0 to in15) signals from different pads of the TRD. It also has 16 output analog signals (out0 to out15). Two signals, one from the in15 of the previous chip to in0 and one from in15 to the in0 of the next chip, are sent in order to be used in the pairing function of the FEE. There are 16 triggering logic signals (adc_cs0 to adc_cs15), which enable the Analog to Digital conversion of the output signal. There are other 16 triggering logic signals, which make the chip-select connection between channels 14 and 0 as well as 15 and 1 of two neighboring chips. An output EVT logic time signal is used in global rate monitoring of transiting analog signals. The chip has two logic signals as inputs: RST (rst_in) used in reseting chip logic and CLK (ocs_in). Voltage references are set through V_{com}, V_{ref} and V_{th}. The four functions are selected through four logic level signals (in-pol-sel, out-sel, tm_mk-sel, nb-en).

2.2 TRD-FEE Interface

Adjacent pad summing is used for position reconstruction. Each pad is of triangular form and depending on which two neighboring ones are used the pairing can be rectangular or tilted (a parallelogram). For summing at the extreme pads, corresponding signals have to be sent to the next chip (Channel 15 of current chip transmits analog signal to channel 0 of next chip.).

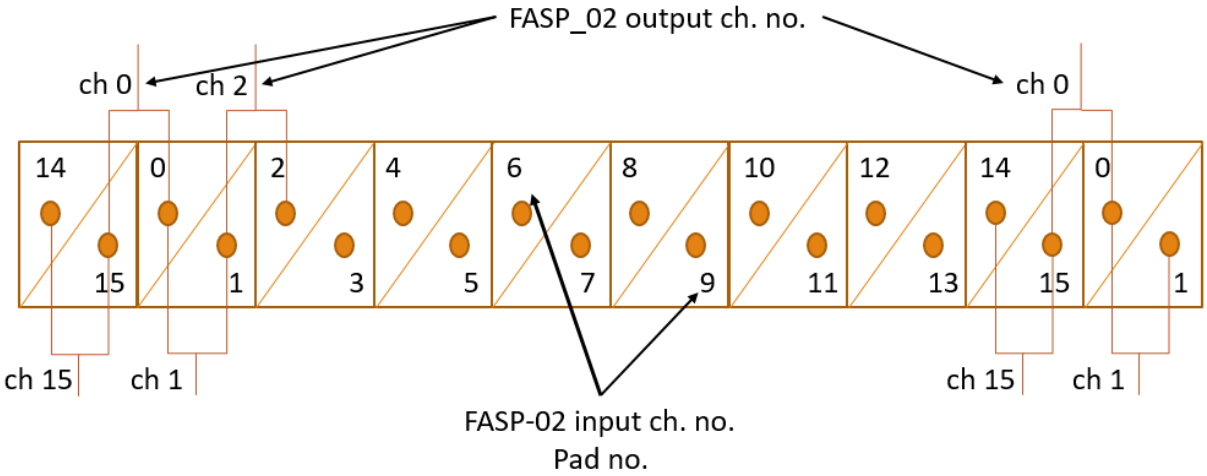

Figure 1: Pad - Input channel connection

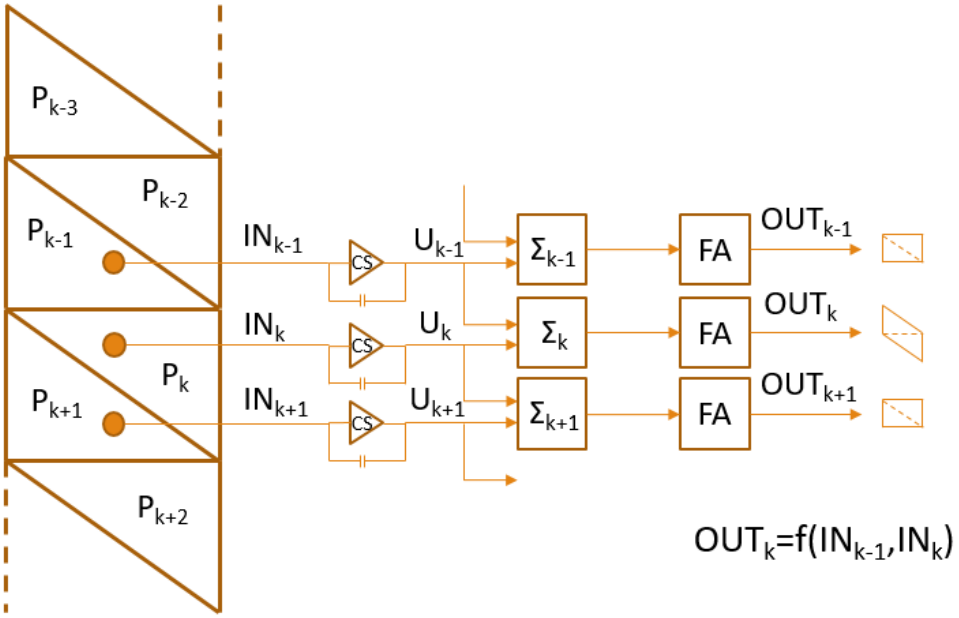

Figure 2: Pairing function: how it is implemented

2.3 FEE-ADC Interface

Analog to digital conversion has three requirements: a good improvement of signal to noise ratio (semi-Gaussian filtering/shaping), a long enough flat signal (flat-top filtering/shaping) and a logic time signal produced along with the analog signal(chip select CS) to activate conversion.

2.4 Trigger transfer function

The trigger transfer function is active when the function nb-en is in the mode EN (enabled). When the output analog signal on channel K is over the threshold, the corresponding CS time signal is transferred to channels K-2 and K+2. The analog signals on these channels will also be flat-topped and transmitted to ADC, independent of the signal amplitude. The signal is transmitted from K to K-2 and K+2 in order to record information on the neighboring pads. If it were K-1 or K+1 the channels used the two triangular pads summed on channel K would be recorded twice.

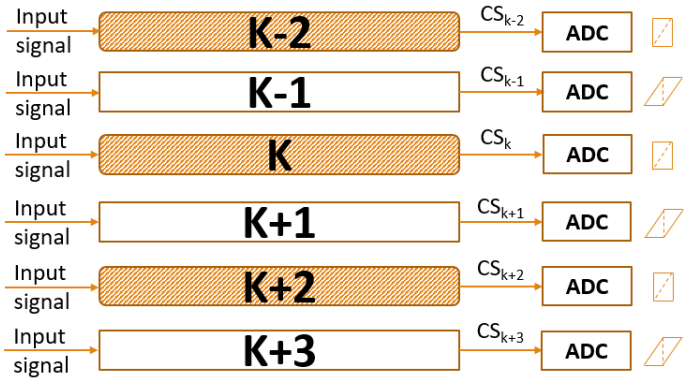

Figure 3: Triggering transfer function. Transmits to the same type of pairing

3 Test Board TB-V2

3.1 Design requirements

The test board must provide: simultaneous testing of two FASP-02 chips; power-supply circuits (3V3A and 3V3D); reference circuits (REF): COM, THR, BL; CLK generation and distribution circuits; manual RST logic signal circuits; test points for all analog and digital signals with local grounding; parameter setting (in-pol-sel, out-sel, tm_mk-sel and nb-en); and connectors for input signals and power supply (+7V).

3.2 PCB Layout

The PCB has four layers: the top contains the components and tracks, the inner layers contain the ground and power distribution respectively for analog and digital circuitries and the base is used as radiators for supply sources.

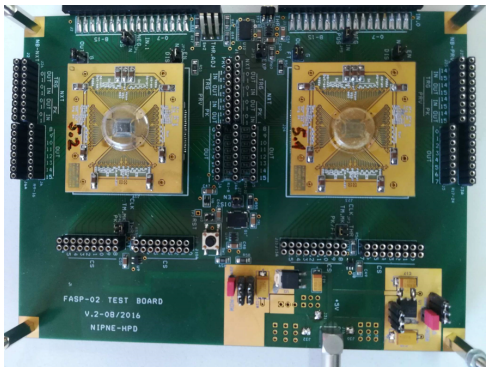

Figure 4: Top layer of the test board

4 TB-V2 measurements

4.1 Threshold DAC calibration

The DAC used for the threshold generator is 8-bit. The reference voltage level was set to 1250 mV. It generates a voltage following the equation:

$$V_{DAC} = 2 \cdot V_{ref} \cdot \frac{N}{256} \tag{1}$$

where N is given by:

$$N = D0 \cdot 2^0 + D1 \cdot 2^1 + D2 \cdot 2^2 + ... + D7 \cdot 2^7 \tag{2}$$

D0,D1,D2,...,D7 being the value of the 8 bits (0 or 1). For the generation of the threshold signal only the bits 1 to 5 were used. First to fourth are being controlled by a 16-step (4-bit) rotary switch and the fifth is controlled with a jumper and is used as a scale expansion. The other bits were set to 0. The measurements have indicated an average step size of 19.6 mV.

Digit	Value	Controller
D0	0	Fixed
D1	0 or 1	Rotary switch
D2	0 or 1	Rotary switch
D3	0 or 1	Rotary switch
D4	0 or 1	Rotary switch
D5	0 or 1	Jumper (Scale EXPand)
D6	0	Fixed
D7	0	Fixed

Figure 5: Table of the DAC setup

Rotary switch position	V_{DAC} (mV) meas (D5=0)	V_{DAC} (mV) meas (D5=1)
0	18	331
1	37	350
2	57	370
3	77	390
4	96	409
5	116	429
6	136	449
7	155	469
8	174	489
9	193	508
A	213	528
B	233	548
C	252	567
D	272	587
E	292	607
F	311	626

Figure 6: DAC measurements

4.2 Other measurements

Other basic measurements have been done. Baseline voltage indicated 298 mV and 297 mV for chip 0 and chip 1 respectively Common voltage was measured to be 990 mV at chip 0 and 987 mV at chip1. Reset was a 3.3 V CMOS logic signal with a duration of 450 ms. The clock was also a 3.3 V CMOS logic signal with a frequency of 40 MHz equivalent of a 25 ns period.

5 TB-V2 and FASP-02 measurements

5.1 DC Power Consumption

The measurement were made under no load (no inputs). From the power scheme the following equations can be deduced.

$$I_{PWR} = I_A + I_D + 2 \cdot I_{STAB} \tag{3}$$

$$I_A = I_{REF} + 2 \cdot I_A^{FASP} \tag{4}$$

$$I_D = I_{CLK} + 2 \cdot I_D^{FASP} \tag{5}$$

The values which can be measured are I_{PWR}, I_A and I_D. The values which need to be calculated are I_{REF},I_{STAB},I_{CLK},I_A^{FASP} and I_D^{FASP}. In order to solve a system with 3 equations and 5 unknowns, different configurations of the setup were used. By using

the test board by itself and the test board and one chip all unknown values can be calculated. Then, by using the test board with two chips, these values can be verified. The final results are: the test board TB-V2 draws 55.7 mA ($I_{REF} + I_{CLK} + 2 \cdot I_{STAB}$) and the chip FASP_02 draws 53.3 mA ($I_A + I_D$).

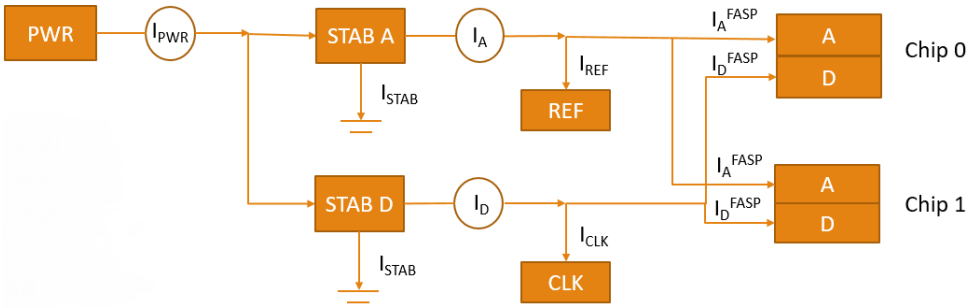

Figure 7: Power scheme

5.2 Working modes testing

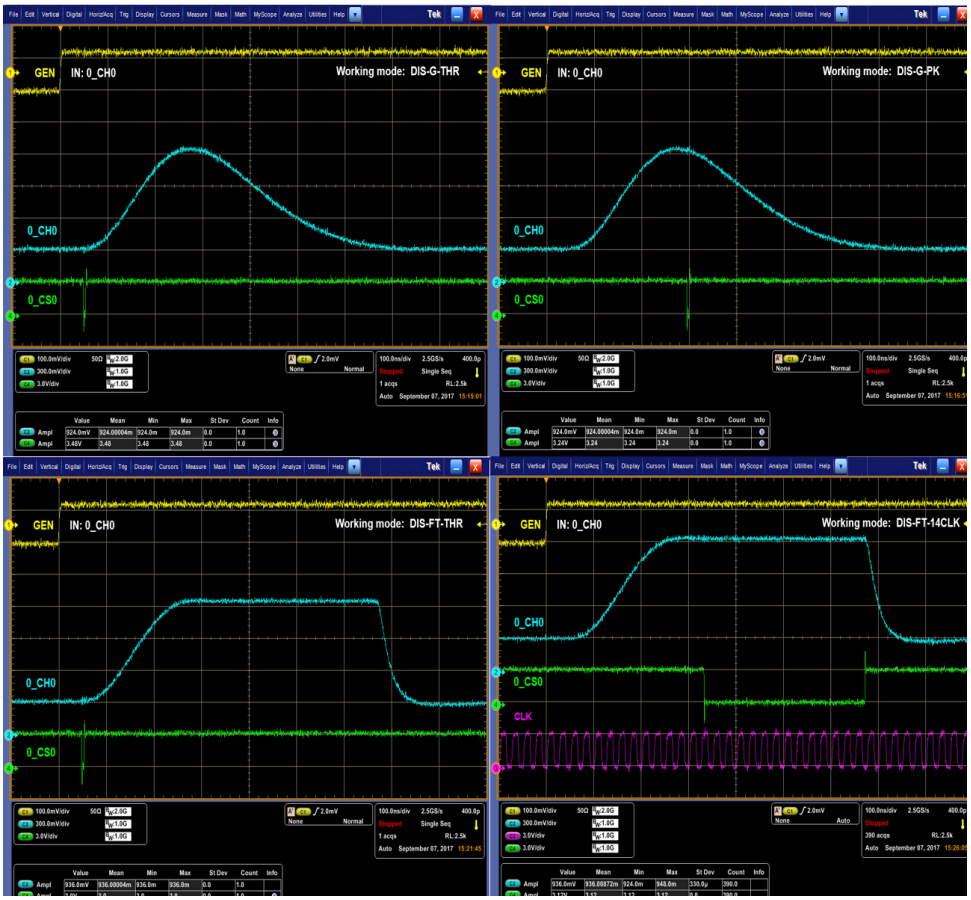

Figure 8: Top: semi-Gaussian with threshold trigger (left) and peak trigger (right); Bottom: flat-top with threshold trigger (left) and 14CLK trigger (right)

The chip has four functions, all of which having two different modes. By taking into account all combinations there are a total of 16 working modes for the chip. Only 8

modes were tested, the polarity of the input being kept positive. The equipment used was the following: waveform generator Keysight 33600A Series[2] , mixed signal oscilloscope Tektronix MSO 5204B[3], dual power supply Toellner TOE 8842[4], test board TB-V2 and a charge injection circuit. The generated signal was a pulse type, with a width of 100 μs, a lead and trail edge of 4 ns and a frequency of 1 kHz. The power supply was set at 7 V. The oscilloscope was in either sample mode or Waveform Database mode (10^6 acquisitions). The threshold was at 96.1 mV (rotary switch step 4, scale expansion disabled). Input channel 15 was set to ground as otherwise the chip would not work properly. The chips used in the testing were: for chip 0 the FASP-02 no. 5.1 and for chip 1 the FASP-02 no. 5.2.

Figure 9: Semi-Gaussian with peak detect

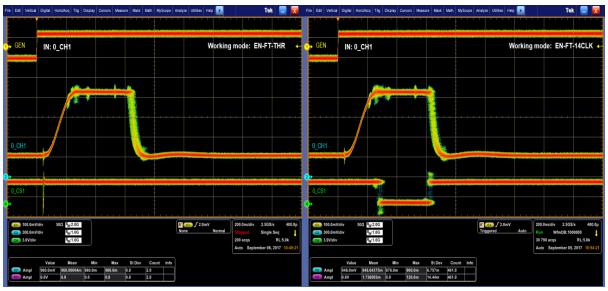

Figure 10: Flat-top on channel 4 (chip 0 left and chip 1 right)

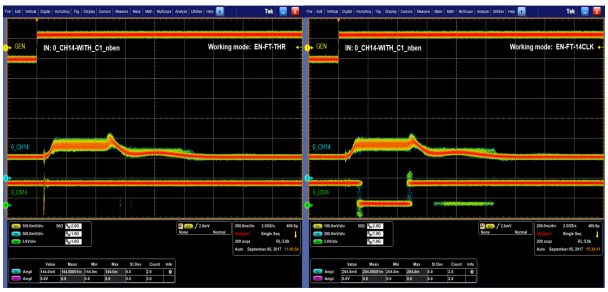

Figure 11: Flat-top on channel 14 (chip 0 left and chip 1 right)

Starting the working modes test, first the neighboring chip select transfer function was disabled. All four cases were working properly.

Next, the testing was done with the neighboring chip select transfer function was enabled. The semi-Gaussian output signal was created properly. The threshold detection

was working correctly, in contrast to the peak detection, which was triggering before the peak itself. Due to the incorrect peak detection, the flat-top signal was also affected, generating the flat-top before the peak itself. The rate of error differed channel-wise, with the most stable being 4 and 11 (the ones in the middle of each of the 8 channel bands), while the most affected were 0, 1, 14 and 15.

Due to the fact that errors appear when the chip select signal is transmitted to neighboring channels and that the most affected are the channels at the edge of the chip, logic signal communication between chips was tested. Taking into account that channel 15 already was grounded only the signals between channel 14 and 0 of the first and second chip respectively could provide information. It was observed that the peak detection signals trigger at the wrong time and also later when there is no signal. These triggers induce transients in the analog signal. The measurements were made also with no input and the logic signals also appeared.

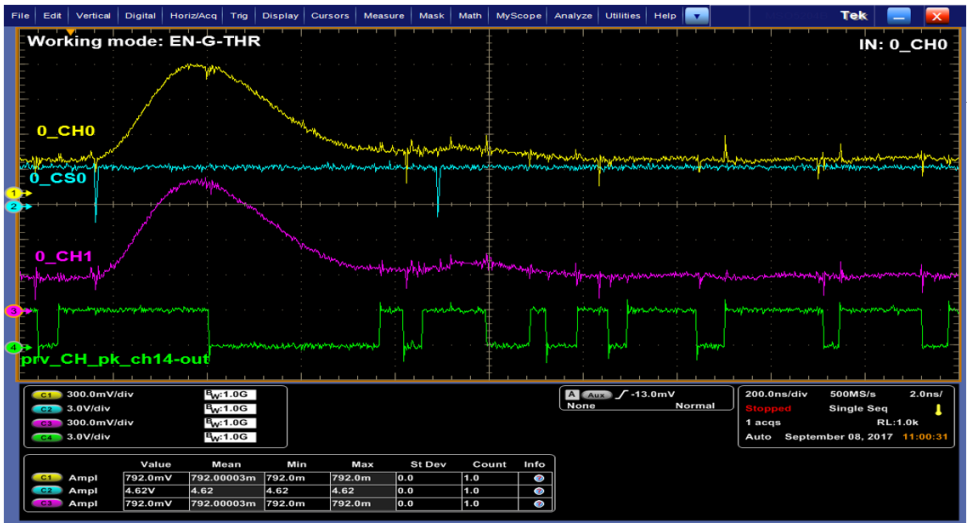

Figure 12: Logic signal between chips inducing transients on analog signal

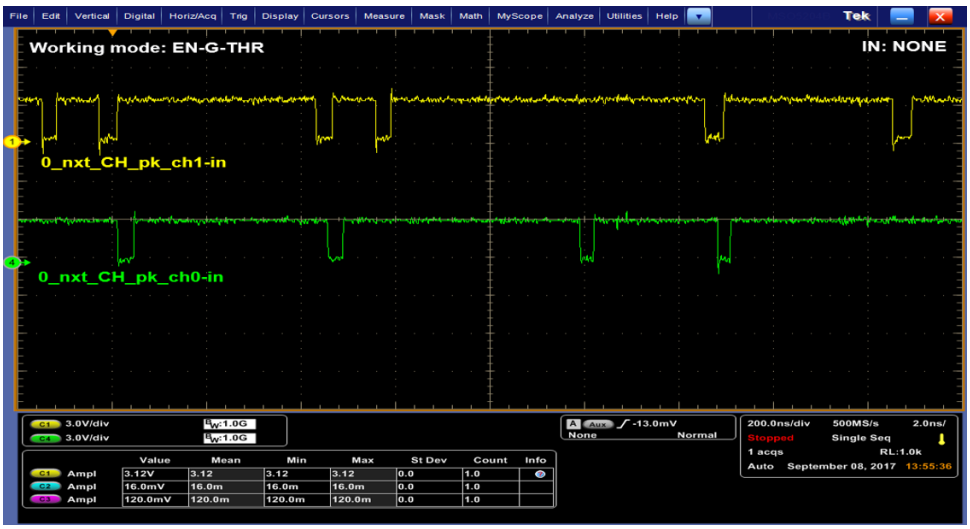

Figure 13: Logic signals generated without input

6 Conclusions

Tests have been done, but not all possible working modes have been covered. Because channel 15 is problematic, communication between chips could not be completely tested. There are problems with flat-top and peak modes when function nb-en is enabled. Some logic signals induce transients in analog signals. Further tests need to be done and the designer of the chip can make further conclusions upon the results.

References

[1] I. Selyuzhenkov and A. Toia, Eds., *CBM progress report 2016*. GSI Helmholtzzentrum für Schwerionenforschung GmbH, 2017, ISBN: 978-3-9815227-4-7.

[2] *33600A Series Trueform Waveform Generators*, USA, Aug. 2014. [Online]. Available: http://literature.cdn.keysight.com/litweb/pdf/5991-3272EN.pdf.

[3] *Mixed Signal Oscilloscopes MSO5000, DPO5000 Series Datasheet*, 2013. [Online]. Available: https://www.tek.com/datasheet/mso5000-dpo5000-series.

[4] [Online]. Available: http://www.toellner.de/html/pages/en-homepage-products-power-supplies-toe8840.htm.

Features of p_T distributions and their $\langle p_{\mathrm{T}} \rangle$ in Au+Au collisions at 7.7 GeV

Avramescu Dana[1,2] and Lindner Amelia[1,2]

[1]IFIN-HH, Hadron Physics Department
[2]University of Bucharest

Abstract

We studied the geometrical scaling between the mean value of the transverse momentum $\langle p_{\mathrm{T}} \rangle$ and a specific quantity suggested by the Colour Class Condensate theory, denoted by $\sqrt{(dN_{ch}/dy)/S_{\perp}}$. This scaling factor is proportional to the density of charged particles over unit of rapidity and the overlapping surface between the two colliding nuclei computed from Glauber Monte Carlo simulations. In order to notice this scaling, the $\langle p_{\mathrm{T}} \rangle$ and the associated errors were computed by fitting the p_T spectra with the Bylinkin function and then extrapolating to the unmeasured regions of p_T values. We also extracted the corresponding core contributions. This study was conducted using data obtained by the STAR experiment (within the BES program at RHIC) in Au+Au collisions at $\sqrt{s} = 7.7$ GeV.

1 Introduction

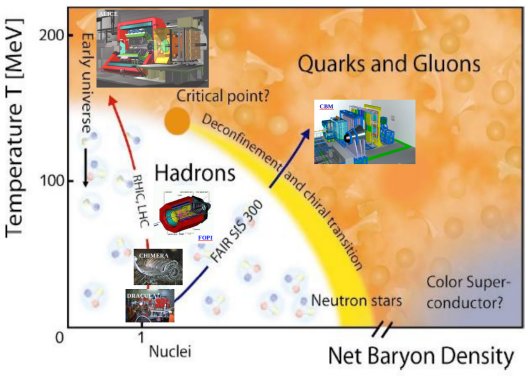

Figure 1: QCD phase diagram and the experiments which are studying it in collaboration with NIHAM.

The major interest in studying heavy-ion collisions comes from the chance to explore the phase structure of hot and dense nuclear matter [1], displayed in the phase diagram of Quantum Chromodynamics (QCD theory of strong interactions) [2] shown in Figure 1. Signatures of deconfined matter were evidenced in high energy heavy-ion collision experiments. Theoretical models predict a QCD phase transition critical point. If this critical point exists, it should appear at the center of mass energies in the range of $\sqrt{s} = 5$-50 GeV [3], recently covered by the Beam Energy Scan (BES) program at RHIC. In order to study the existence of the QCD's critical point, we have started our analysis with data obtained at STAR, within the BES program, for the lowest center of mass energy of $\sqrt{s} = 7.7$ GeV obtained with

this experiment [4]. In the framework of the color glass condensate theory, certain bulk observables behave in a specific manner, being geometrically scaled [5]. This picture naturally leads to the concept of gluon saturation, which is expected to be observed at higher energies, as those that can be provided by the Large Hadron Collider (LHC). In order to take into account the geometry of the system, we chose to study the dependence of $\langle p_{\mathrm{T}} \rangle$ (the mean value of the magnitude of the transverse momentum) with $\sqrt{(dN_{ch}/dy)/S_{\perp}}$, where $S_{\perp}$ is the transverse overlap surface between the two colliding nuclei.

2 Data analysis

2.1 Fitting procedure

The fitting process was conducted by trying various functions used in the literature, in order to investigate which one gives a better data to fit ratio.

The spectra were fitted with a Boltzmann distribution [4], derived from thermodynamic considerations, assuming that the produced particles are emitted by a system in thermal equilibrium, characterized by Boltzmann-Gibbs statistics:

$$\frac{1}{2\pi p_T}\frac{d^2N}{dydp_T} = Nm_T e^{-\frac{m_T}{T}} \tag{1}$$

where $m_T = \sqrt{p_T^2 + m^2}$ is the transverse mass, T is the equilibrium thermodynamic temperature and N is a normalization constant.

The fitting procedure was continued with an exponential function in p_T [4] mainly used at higher values of p_T and a power-law term which successfully describes the high p_T region of the particle spectra, but fails in the region of low p_T where the spectra exhibits a more exponential shape:

$$\frac{1}{2\pi p_T}\frac{d^2N}{dydp_T} = Ne^{-\frac{p_T}{T}} \tag{2}$$

$$\frac{1}{2\pi p_T}\frac{d^2N}{dydp_T} = N\left[1 + \left(\frac{p_T}{T^2}\right)^2\right]^n \tag{3}$$

In order to take into account the deviation of the system from extensive thermodynamic equilibrium, the Tsallis distribution was used. It is generalized form of the Boltzmann-Gibbs entropy [6] and can be expressed as:

$$\frac{1}{2\pi p_T}\frac{d^2N}{dydp_T} = N\frac{(n-1)(n-2)}{nT(nT + m(n-2))}\left(1 + \frac{m_T - m}{nT}\right)^{-n} \tag{4}$$

where q is the nonextensivity parameter. In the limit $q \to 1$ the Tsallis function becomes a Boltzmann-Gibbs distribution. For values of $q \neq 1$, the Tsalis function behaves like a power law function with $n = -1/(1-q)$.

In order to include the colective behavior of the emitting source, the spectra was fitted with a Boltzmann-Gibbs Blast Wave function [7], which is based on hydrodynamic considerations and takes into account the expansion of the fireball:

$$\frac{1}{2\pi p_T}\frac{d^2N}{dydp_T} \propto \int_0^R rdrm_T I_0\left(\frac{p_T \sinh\rho}{T_{kin}}\right) K_1\left(\frac{m_T \cosh\rho}{T_{kin}}\right) \tag{5}$$

where ρ represents the velocity profile:

$$\rho = \tanh^{-1}\beta_T = \tanh^{-1}\left[\left(\frac{r}{R}\right)^n \beta_s\right] \tag{6}$$

and I_0 and K_1 are modified Bessel functions of first and second order, R gives the size of the system, β_T is the parametrization of the transverse expansion velocity, β_S is the transverse velocity at the freeze-out surface and T_{kin} represents the temperature at kinetic freeze-out.

In high-energy heavy-ion collisions, the hadroproduction can be described by two distinct mechanisms [12, 13]. The Bylinkin function (Eq. 7) describes fenomenologically these mechanisms and, according to [8], the spectra of charged hadrons produced in collisions can be approximated as a sum of an exponential and a power-law term which depend on the produced hadron transverse momentum.

The particles having lower values of p_T are considered to originate from the so called "quark-gluon soup" and thus can be very well described by an p_T exponential function (Boltzmann-like), while those characterized by higher values of p_T come from mini-jets which, after passing through the nuclei, suffer a process of hadronization and are described by a power-law function. Combining these two mechanisms, the following expression is obtained [8]:

$$\frac{1}{2\pi p_T}\frac{d^2N}{dydp_T} = A_e e^{-\frac{m_T - m}{T_e}} + A\left[1 + \frac{1}{n}\left(\frac{p_T}{T}\right)^2\right]^{-n} \tag{7}$$

where A_e, A, T_e, T, n are the free fit parameters. An example of the fits, using the above mentioned functions may be seen in Figure 2.

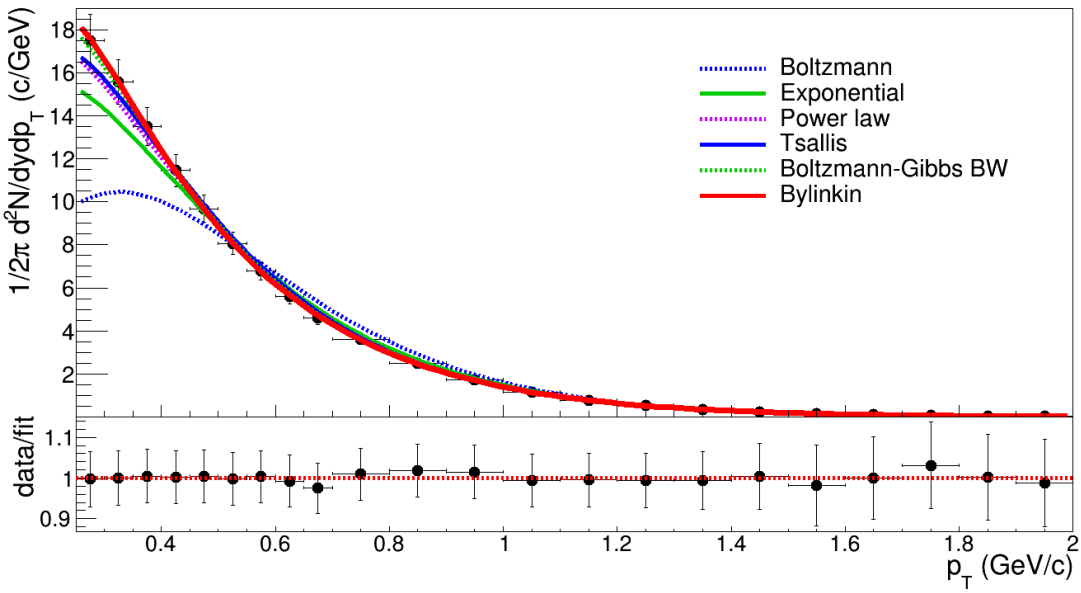

Figure 2: *Top*: Example of π^+ spectra at 0-5% centrality [4] fitted with Boltzmann (1), exponential (2), power-law (3), Tsallis (4), Boltzmann-Gibbs blast wave (5) and Bylinkin (7) functions *Bottom*: Ratio between the data and the corresponding fit performed with the Bylinkin function.

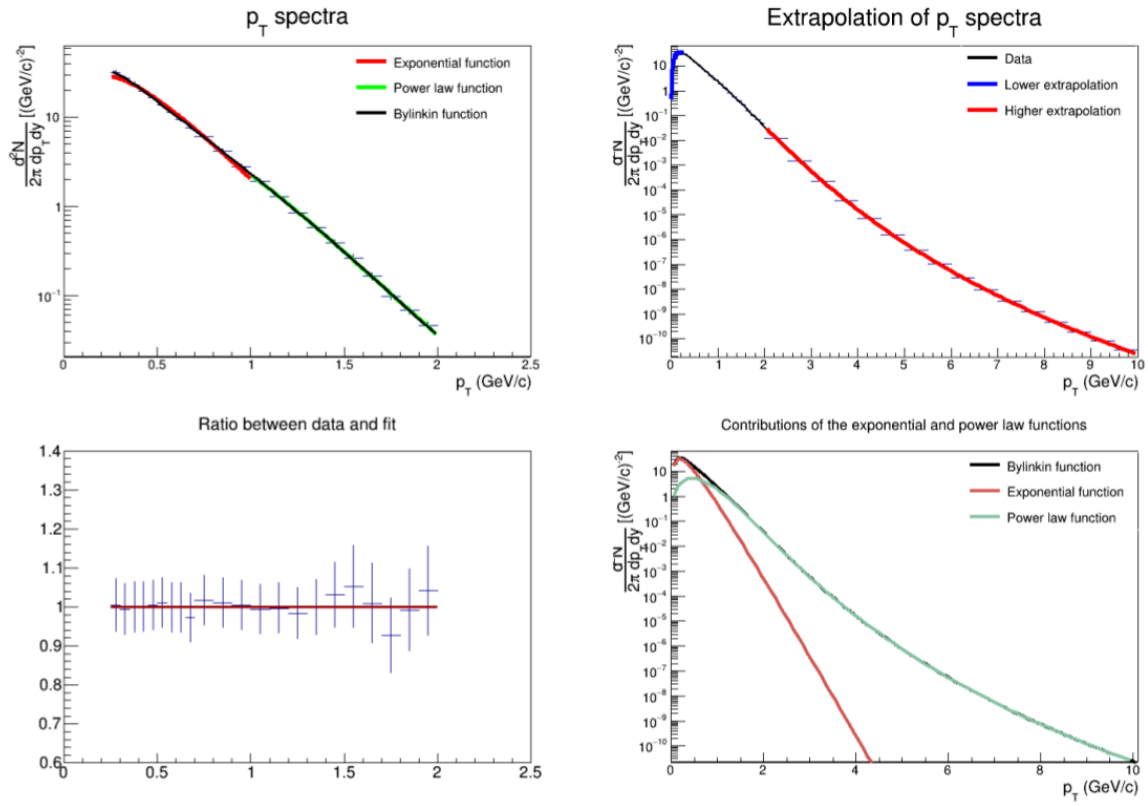

Figure 3: An example of the method used for the fit procedure for π^- in the 0-5% centrality bin.

2.2 Extracting $\langle p_{\mathrm{T}} \rangle$

Due to the large number of parameters involved, the fit with the Bylinkin function was very sensitive to the initialization of the parameters. In order to assure the stability of the fit, the spectra was fitted only with the exponential term up to 1 GeV/c and afterwards with the power-law term starting from 1 GeV/c (Figure 3, *Top-left*). The obtained parameters were provided as input for the Bylinkin distribution. The 1 GeV/c limit was chosen according to [8]. This value is the limit up to which the exponential contribution is significant and from which the power-law term becomes relevant. The fitted spectra and the fit quality can be observed in Figure 4.

The method used for this study consists in fitting the transverse momentum spectra $d^2N/2\pi dp_T dy$ at a given centrality and with the Bylinkin function given by Equation 7, as can be seen in Figure 3 (*Top-left*). The fit quality given by the ratio between the data and fit is shown in Figure 3 (*Bottom-left*). In order to take into account the unmeasured regions, each spectrum has been extrapolated using the fit result with the fit function in the unmeasured p_T regions, as shown in Figure 3 (*Top-right*). Extrapolating the spectra higher than 10 GeV/c does not have a strong influence on the value of the $\langle p_{\mathrm{T}} \rangle$. From the obtained extrapolated spectrum, the mean value of the transverse momentum $\langle p_{\mathrm{T}} \rangle$ can be estimated. The contributions of the exponential and the power-law terms are represented in Figure 3 (*Bottom-right*).

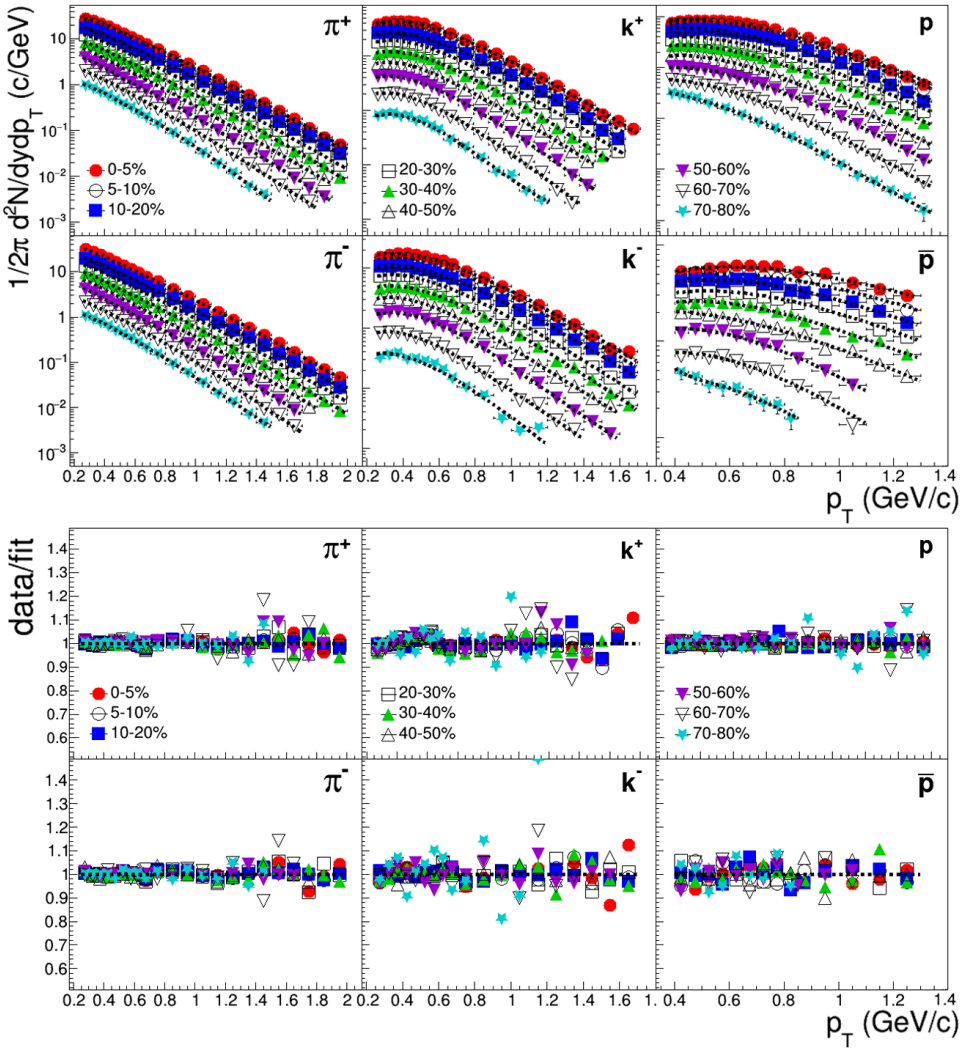

Figure 4: *Top*: Spectra of π^+ [4] at various centralities fitted with the Bylinkin function. *Bottom*: The ratio between data and the corresponding fit with the Bylinkin function for π^+ at different centralities.

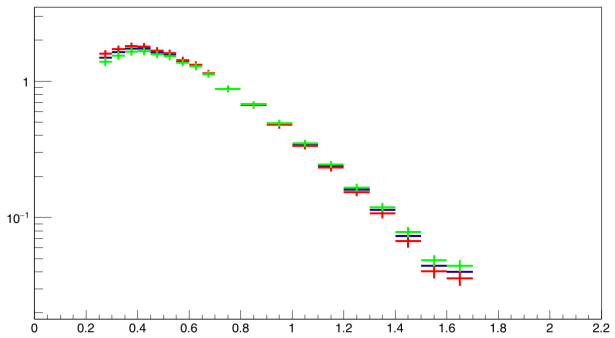

Figure 5: The method used in this study for estimating $\langle p_{\mathrm{T}} \rangle$ uncertainty.

The method described above and used for the estimation of the $\langle p_{\mathrm{T}} \rangle$ does not take into account the systematic errors propagated through the parameters of the fit function. In this case, the method of estimating the $\langle p_{\mathrm{T}} \rangle$ errors consists in shifting the first half of the spectra within the upper zone of the statistical and systematic error values with respect to the weighted contribution of the error up to the middle of the spectra, while the other half of the spectra is being shifted within the lower values of the errors and vice-versa. The errors considered are obtained from the difference between the new values divided by 2 (Figure 5). The errors estimated with this method have a small contribution relative to those

obtained in [4], where the systematic uncertainty is obtained by extrapolating the spectra with multiple fit functions. The values obtained for $\langle p_T \rangle$ values with the described procedure are represented in Figure 6.

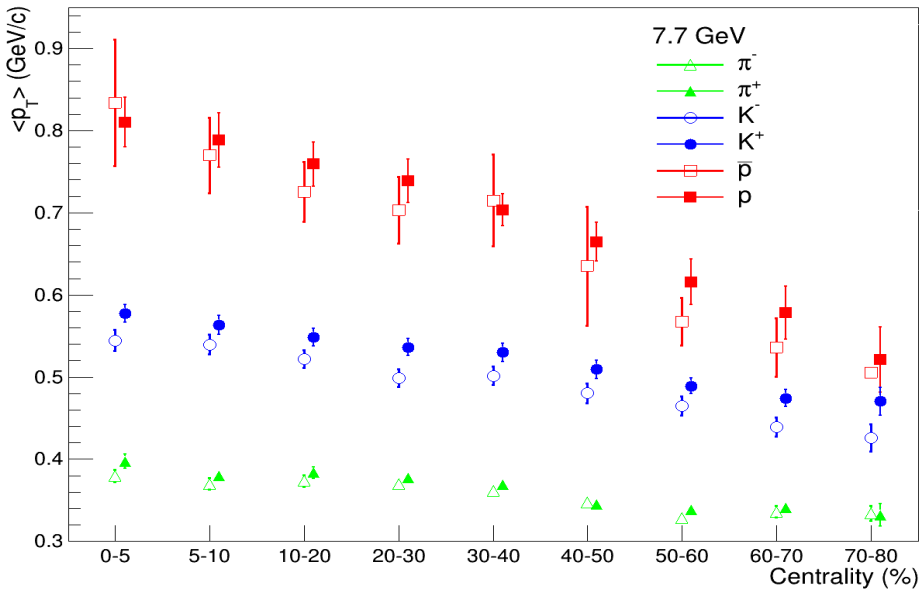

Figure 6: $\langle p_T \rangle$ as a function of centrality (pions, kaons, protons and their antiparticles).

In order to crosscheck the results, a comparison between the obtained values and those extracted from [4] was performed. The $\langle p_T \rangle$ values were artificially shifted in centrality in order to have a better representation of the compared results. One can see that the results obtained are very similar to those in [4], which implies a good behaviour of the fit function and of the used method (Figure 7). It can be noticed in Figure 7 that the obtained $\langle p_T \rangle$ values are decreasing from central to peripheral collisions for all the particles studied.

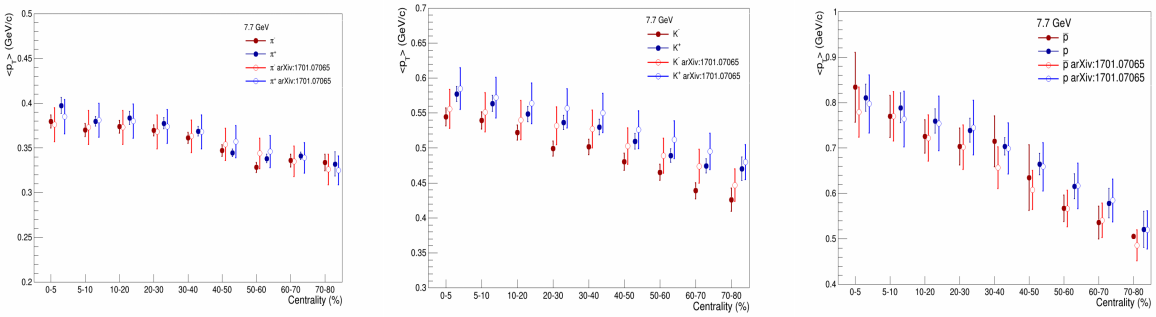

Figure 7: $\langle p_T \rangle$ as a function of centrality compared with the published results [4] for pions (left), kaons (middle), protons (right) and their antiparticles.

3 $\langle p_{\mathrm{T}} \rangle$ as a function of $\sqrt{(dN_{ch}/dy)/S_{\perp}}$

3.1 Color Glass Condensate considerations

Color Glass Condensate [14] (CGC) is a QCD inspired effective theory in which the classical fields have the main role. CGC aims for a description of the small x part of the hadron wave function used to calculate processes determined by small x partons.

Within this approach, $\langle p_{\mathrm{T}} \rangle / \sqrt{(dN_{ch}/dy)/S_{\perp}}$ is expected de decrease towards central collisions as a signature for gluon saturation. Therefore, such a representation as a function of centrality for different collision energies for existing experimental data could help in understanding the properties of small x regime.

The transverse overlap surface of the two colliding nuclei can't be directly measured, therefore other related considerations need to be involved and they are based on Glauber model.

3.2 Glauber Monte Carlo

The Glauber model [10] is mainly used to describe the centrality of a certain event by computing geometrical quantities not accessible by direct experimental measurements, like the average impact parameter $\langle b \rangle$, the number of participating nucleons N_{part}, the number of binary nucleon-nucleon collisions N_{coll}, nuclear overlap function T_{AB}, eccentricity ϵ and, what is of interest for our study, the overlap surface $S_{\perp}$.

In the Glauber Monte Carlo (GMC) simulations, this is done by distributing nucleons in the two colliding nuclei in a three-dimensional coordinate system accordingly to a Woods-Saxon distribution describing the nuclear density profile system and then randomly extracting an impact parameter from this distribution as $d\sigma/db = 2\pi b$. Nucleons are assumed to travel on straight line trajectories, whether they collide or not, the inelastic nucleon-nucleon cross-section is assumed to be independent of the number of collisions a nucleon underwent before and the collision only occurs if the distance between nucleons is smaller than $\sqrt{\sigma_{inel}^{NN}/\pi}$.

In this study, two types of overlapping surfaces were used: $S_{geometrical}$ calculated from geometrical considerations by simply computing the overlap surface between two circles having the same radius and placed at a distance equal to the impact parameter provided from the GMC simulations and $S_{variance}$ which corresponds to a transverse area:

$$S_{variance} \sim \sqrt{\sigma_x^2 \sigma_y^2} - \sigma_{xy} \tag{8}$$

where $\sigma_x^2 =< x^2 > - < x >^2$ and $\sigma_{xy} =< xy > - < x >< y >$ (x and y represent the projections of the radius on the X and Y axes).

3.3 Geometrical scaling

The density of charged particles over unit of rapidity was obtained by taking the integrated yield per particle from [4] and then performing the following summation for each individual particle:

$$\frac{dN_{ch}}{dy} = \sum_i \frac{dN_i}{dy} \tag{9}$$

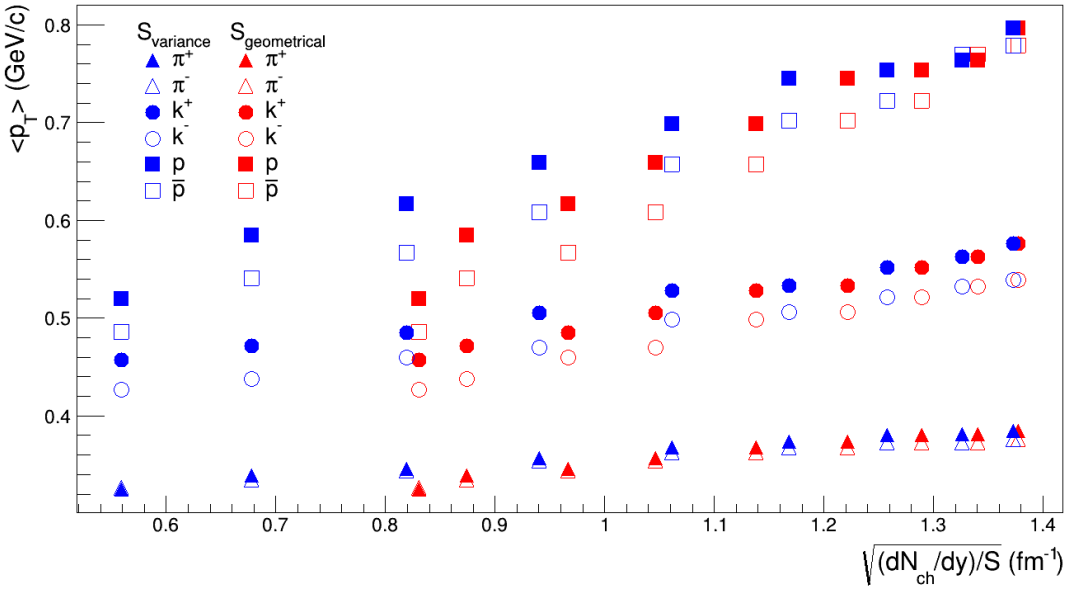

Figure 8: The geometrical scaling between $\langle p_{\mathrm{T}} \rangle$ and $\sqrt{(dN_{ch}/dy)/S_{\perp}}$, estimated considering $S_{geometrical}$ and $S_{variance}$ for pions, kaons, protons and their corresponding antiparticles.

where i is used to index the involved particles: pions, kaons, protons and antiparticles. The obtained results scaled with the two calculated surfaces from GMC may be seen in Figure 8.

3.4 Core-corona interplay

All the calculations were done under the assumption that all the nucleons of a nuclei are at statistical thermodynamic equilibrium, which is not the case. The nucleons placed close to the surface of interaction between the two colliding nuclei suffer less collisions than those from the center region such that they won't reach thermal equilibrium and only scatter once, being similar to those observed in minimum bias proton-proton collisions. Therefore, the spectra can be analyzed as being composed from two distinct regions whose relative fractions depend on centrality: the core, consisting of quarks and gluons at statistical equilibrium, and the corona, represented by the nucleons which only suffer single collisions.

The fraction of core f_{core} and corona $f_{corona} = 1 - f_{core}$ particles as a function of centrality have also been calculated using the Glauber Monte Carlo approach. In the core-corona model, the centrality dependence of the experimental yield of a given particle i in a centrality bin containing N_{part} participants, over unit of rapidity is given by:

$$\left(\frac{dN}{dy}\right)_i^{exp} = N_{part}\left[(1 - f_{core})M_i^{ppMB} + f_{core}M_i^{core}\right] \tag{10}$$

where M_i^{core} is the multiplicity per core participant and $M_i^{ppMB} = M_i^{corona}$ is the multiplicity per corona participant, corresponding to the minimum-bias proton-proton collisions.

The value of M_i^{ppMB} can be determined either from integrated fits or using already published data. Since we were not able to find these values for our energy of interest, we estimated them based on the measured data for other energies. From Figure 9 *(Left)*,

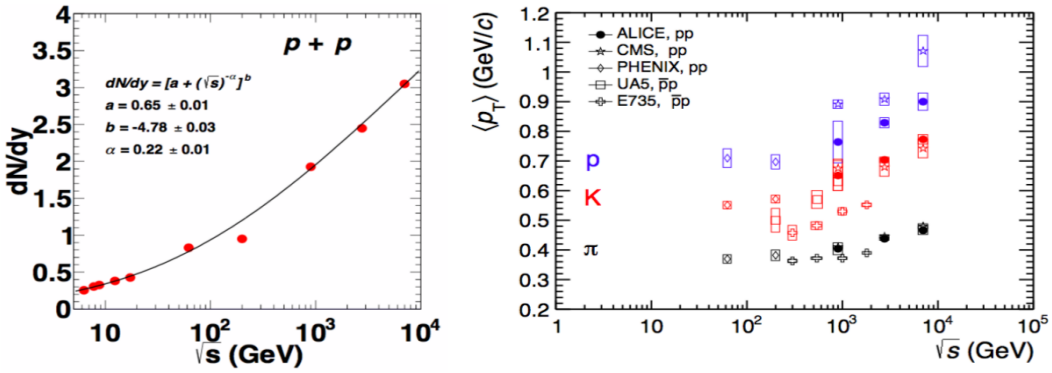

Figure 9: *Left*: The variation of the integrated yield dN/dy for charged pions as a function of $\sqrt{s}$. The solid curve represents the parameterization $(a + \sqrt{s}^{-\alpha})^b$ [11]. *Right*: $\langle p_{\mathrm{T}} \rangle$ as a function of the centre-of-mass energy. Errors (open boxes) are the combination of statistical (negligible) and systematic uncertainties. Normalization uncertainties are not included [15].

using the given parametrization, the corresponding minimum-bias yield for pions at 7.7 GeV can be calculated. Afterwards, M_i^{core} can be calculated by using Equation (10) for the most central multiplicity bin. The experimental value for p_T can be decomposed as:

$$< p_T >_i^{exp} = \frac{f_{core} < p_T >_i^{core} M_i^{core} + (1 - f_{core}) < p_T >_i^{ppMB} M_i^{ppMB}}{f_{core} M_i^{core} + (1 - f_{core}) M_i^{ppMB}} \tag{11}$$

from which the core correspondent can be calculated. From Figure 9 *(Right)*, the value of $< p_T >^{ppMB}$ only for π^- can be extracted.

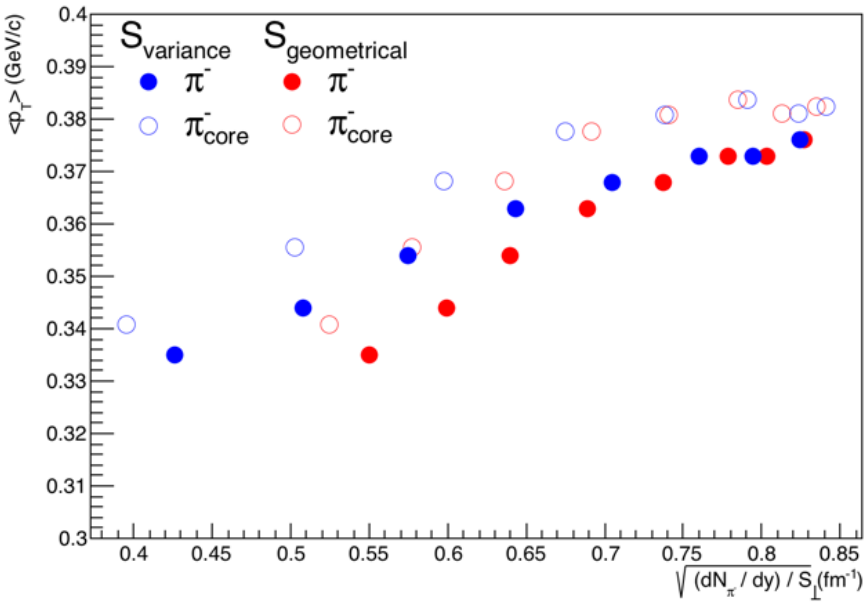

Figure 10: The geometrical scaling between $\langle p_{\mathrm{T}} \rangle$ and $\sqrt{(dN_{\pi^-}/dy)/S_\perp}$ and the corresponding core contribution for π^-.

By performing the above scaling of $\langle p_{\mathrm{T}} \rangle$ with respect to $\sqrt{(dN_{\pi^-}/dy)/S_\perp}$ and then calculating the corresponding core contributions for $< p_T^{core} >$ as a function of $\sqrt{(dN_{\pi^-}/dy)^{core}/S_\perp^{core}}$, where $S_\perp^{core}$ was also obtained via Glauber MC, we get the results shown in Figure 10.

4 Conclusions and perspectives

Our preliminary results show that:

• The dependence of $\langle p_{\mathrm{T}} \rangle$ as a function of $\sqrt{(dN_{ch}/dy)/S_\perp}$ is linear;

• There is no indication of change of the slope with the centrality considering the $\sqrt{(dN_{ch}/dy)/S_\perp}$ for all the particles, at the lowest measured energy of 7.7 GeV.

• In the $\sqrt{(dN_{\pi^-}/dy)/S_\perp}$ representation there is a tendency of levelling off towards central collisions which is still under investigation.

5 Acknowledgements

We would like to give special thanks to Prof. Dr. Mihai Petrovici for providing us the chance to work in such an outstanding environment and constantly guiding us, to Dr. Cristian Andrei and Dr. Andrei Herghelegiu for having the astonishing and sisyphic patience to walk us through the process of learning ROOT, to Dr. Amalia Pop and Madalina Tarzila for taking their time to answer all our questions and provide us their various results and procedures and not last, to the whole HPD team for making our stay extremely enjoyable.

References

[1] M.M. Aggarwal et al. and STAR Collaboration, *An Experimental Exploration of the QCD Phase Diagram: The Search for the Critical Point and the Onset of Deconfinement*, arXiv:1007.2613, 2010

[2] X. Luo, *Exploring the QCD Phase Structure with Beam Energy Scan in Heavy-ion Collisions*, Nuclear Physics A 956, 2016, 75–82

[3] T. Satogata and et al., *RHIC Low-Energy Challenges and Plans*, PoSCPOD07:051, 2007

[4] STAR Collaboration, *Bulk Properties of the Medium Produced in Relativistic Heavy-Ion Collisions from the Beam Energy Scan Program*, arXiv:1701.07065, 2017

[5] T.Lappi, *Energy dependence of the saturation scale and the charged multiplicity in pp and AA collisions*, arXiv:1104.3725, 2011

[6] PHENIX Collaboration, *Measurement of neutral mesons in p+p collisions at* $\sqrt{s}$*=200 GeV and scaling properties of hadron production*, arXiv:1005.3674, 2010

[7] P. J. Siemens. J. O. Rasmussen, *Evidence for a Blast Wave from Compressed Nuclear Matter*, Phys. Rev. Lett. 42, 1979, 880

[8] Nadezda Chernyavskaya, Alexander Bylinkin, Andrey Rostovtsev, *Two Component Model with collective Flow for Hadroproduction in heavy-ion Collisions*, http://dx.doi.org/10.3204/DESY-PROC-2014-04/47

[9] A. A. Bylinkin, A. A. Rostovtsevy, *Comparative Analysis of Pion, Kaon and Proton Spectra Produced at PHENIX*, arXiv:1203.2840, 2012

[10] Michael L. Miller, Klaus Reygers, Stephen J. Sanders, Peter Steinberg, *Glauber Modeling in High Energy Nuclear Collisions*, arXiv:nucl-ex/0701025, 2007

[11] Priyanka Sett, Prashant Shukla, *Pion p_T spectra in p+p collisions as a function of $\sqrt{s}$ and event multiplicity*, arXiv:1408.1034, 2014

[12] A.A. Bylinkin, A. A. Rostovtsev, *Universality of identified hadron production in pp collisions*, Eur. Phys. J. C 74:2898 (2014)

[13] A.A. Bylinkin, A. A. Rostovtsev, *Systematic studies of hadron production spectra in collider experiments*, arXiv:1008.0332 [hep-ph]

[14] F. Gelis, *The Color Glass Condensate*, Ann. Rev. Nucl. Part. Sci. 60, 2010

[15] ALICE Collaboration, *Measurement of pion, kaon and proton production in proton-proton collisions at $\sqrt{s}$=7 TeV*, arXiv:1504.00024, 2015

Weak interaction rates for exotic nuclei relevant in nuclear astrophysics

Mare Adrian Sorin[1,2]

[1]IFIN-HH, Hadron Physics Department
[2]University of Bucharest

1 Introduction

Proton rich nuclei situated in the A$\sim$70 mass region and neutron rich in the A$\sim$100 are investigated theoretically and experimentally because of their properties relevant for astrophysical nucleosynthesis. These nuclei manifest exotic nuclear structure and dynamics generated by the interplay between shape coexistence and mixing, competing neutron-neutron, proton-proton and neutron-proton paring correlations. The β decay properties of the low-lying excited states of proton-rich nuclei situated on the *rp-process* path may be of particular importance because of their thermal population that may influence their effective half-lives at the high temperatures of x-ray bursts.

The *complex* Excited Vampir approach allow for a unified description of the structure and dynamics at low and high spins including in the symmetry projected mean fields neutron-proton correlations in both T=1 and T=0 channels and general two-nucleon unnatural-parity correlations. The beyond-mean-field *complex* Excited Vampir model allows to realistically describe the characteristic features of nuclei in the A=60 to A=90 mass region like shape coexistence and mixing and the strong variation of the deformation with number of nucleons, increasing spin, and excitation energy. Because the Vampir approaches enable the use of large model spaces and general two-body interactions, large-scale nuclear structure studies go far beyond the abilities of the conventional shell-model configuration-mixing approaches.

2 Theoretical Framework

2.1 Complex Excited Vampir model

The *complex* Excited Vampir approach uses the most general Hatree-Fock-Bogoliubov (HFB) vacua as basic building blocks being restricted only by time-reversal and axial symmetry. The HFB transformations are *complex* and mix proton with neutron states as well as states of different parity and angular momentum. This HFB vacua account for arbitrary two-nucleon correlations and simultaneously describe like-nucleon as well as isovector and isoscalar neutron-proton pairing correlations. The broken symmetries are restored by projection before variation and the resulting symmetry-projected configurations are used as test wave-functions. The Vampir solutions, representing the optimal

mean-field description of the yrast states by single symmetry-projected HFB determinants are obtained. Then the Excited Vampir approach is used to construct additional excited states by independent variational calculations. The final solutions are then obtained, for each considered symmetry , by diagonalizing the residual interaction between the successively constructed orthogonal many-nucleon Excited Vampir configurations.

For the A=70 mass region the model uses ^{40}Ca core with the model space being built out of the $1p_{1/2}$, $1p_{3/2}$, $0f_{5/2}$, $0f_{7/2}$, $1d_{5/2}$ and $0g_{9/2}$ oscillator orbits for the valence protons and neutrons. A large model space above the ^{40}Ca core is used for the A=100 region that includes $1p_{1/2}$, $1p_{3/2}$, $0f_{5/2}$, $0f_{7/2}$, $2s_{1/2}$,$1d_{3/2}$, $1d_{5/2}$, $0g_{7/2}$, $0g_{9/2}$ and $0h_{11/2}$ oscillator orbits for the valence protons and neutrons. Using this large model space the model successfully describes shape coexistence phenomena for neutron-rich A$\sim$100 nuclei, including Gamow-Teller(GT) strength distributions and beta-delayed neutron emission probabilities [1,2,3].

2.2 Weak Interaction Processes

In the four-vector current representation of weak interactions the current

$$j_\mu(r) = (j_\mu(r))_{hadr} + j_\mu(r)_{lept} \tag{1}$$

consists of a hadronic and leptonic part [4]. All weak interaction processes can be described within the self coupling of the four-vector current. The interaction can then be written as:

$$H' = k \int j_\mu^\dagger(r) j_\mu(r)$$

$$= k\{\int (j_\mu^\dagger(r))_{lept}(j_\mu(r))_{lept} d^3r + \left(\int (j_\mu^\dagger(r))_{hadr}(j_\mu(r))_{lept} + H.c\right) +$$

$$+ \int (j_\mu^\dagger(r))_{hadr}(j_\mu(r))_{hadr}\} \tag{2}$$

Beta decay processes are caused by leptonic-hadronic current interaction(middle term of the Hamiltonian) and are classified as follows:

$$(Z, A) \rightarrow (Z+1, A) + e^- + \bar{\nu_e} \leftrightarrow \beta^-\text{decay}$$

$$(Z, A) \rightarrow (Z-1, A) + e^+ + \nu_e \leftrightarrow \beta^+\text{decay}$$

$$e^- + (Z, A) \rightarrow (Z-1, A) + \nu_e \leftrightarrow e^-\text{capture}$$

$$\nu_e + (Z, A) \rightarrow (Z+1, A) + e^- \leftrightarrow \text{inverse } \beta$$

$$\bar{\nu_e} + (Z, A) \rightarrow (Z-1, A) + e^+ \leftrightarrow \text{inverse } \beta$$

There are two matrix elements contributing in the case of allowed transitions and six for the first-forbidden transitions as seen in Table 1 [5,6].

Allowed	
$M(\rho_v, \lambda = 0)$	$c_V \int 1$
$M(j_A, \kappa = 0, \lambda = 1)$	$c_A \int \vec{\sigma}$
First Forbidden	
$M(\rho_A, \lambda = 0)$	$c_A \int \gamma_5$
$M(j_A, \kappa = 1, \lambda = 0)$	$c_A \int \vec{\sigma} \cdot \vec{r}$
$M(\rho_V, \lambda = 1)$	$c_V \int \vec{r} i$
$M(j_V, \kappa = 0, \lambda = 1)$	$c_V \int \vec{\alpha}$
$M(j_A, \kappa = 1, \lambda = 1)$	$c_A \int \vec{\sigma} \times \vec{r}$
$M(j_A, \kappa = 1, \lambda = 2)$	$c_A \int i B_{ij}$

Table 1. *Allowed and first-forbidden nuclear matrix elements*

The Fermi and Gamow-Teller reduced transition probabilities can be written as:

$$B_{if}(F) = \frac{1}{2J_i + 1} \left| \mathcal{M}_F \right|^2 \tag{3}$$

$$B_{if}(GT) = \frac{1}{2J_i + 1} (\frac{g_A}{g_V})^2 \left| \mathcal{M}_{GT} \right|^2 \tag{4}$$

with g_A/g_V = -1.26. The Fermi and Gamow-Teller nuclear matrix elements between initial ($|\xi_i J_i\rangle$) and final ($|\xi_f J_f\rangle$) *complex* Excited Vampir wave functions [7] of states of spin J_i, J_f respectively,

$$\mathcal{M}_F \equiv (\xi_f J_f || \widehat{1} || \xi_i J_i) =$$

$$= \delta_{J_i J_f} \sum_{ab} M_F(ab) \left\langle \xi_f J_f || \left[c_a^\dagger \tilde{c}_b \right]_0 || \xi_i J_i \right\rangle \tag{5}$$

$$\mathcal{M}_{GT} \equiv (\xi_f J_f || \widehat{\sigma} || \xi_i J_i) =$$

$$= \sum_{ab} M_{GT}(ab) \left\langle \xi_f J_f || \left[c_a^\dagger \tilde{c}_b \right]_1 || \xi_i J_i \right\rangle \tag{6}$$

are composed of the reduced single-particle matrix elements of the unit operator 1, $M_F(ab) = (a|\widehat{1}||b)$, and Pauli spin operator σ, $M_{GT}(ab) = (a||\widehat{\sigma}||b)$, and the reduced one body transition densities calculated using harmonic oscillator wave functions. For β^-, $c_a^\dagger$ is the proton creation operator and $\tilde{c}_b$ is the neutron annihilation operator.

An example of theoretical Fermi strength distribution is depicted in Figure 1 for the decay of the ground state of ^{74}Sr to the daughter states in ^{74}Rb. The calculated Gamow-Teller decay half-life of ^{74}Sr under terrestrial conditions is 137 ms and for the Fermi decay is 48 ms. Thus the theoretical half-life of 36 ms is in good agreement with the available experimental value of 27 ms.

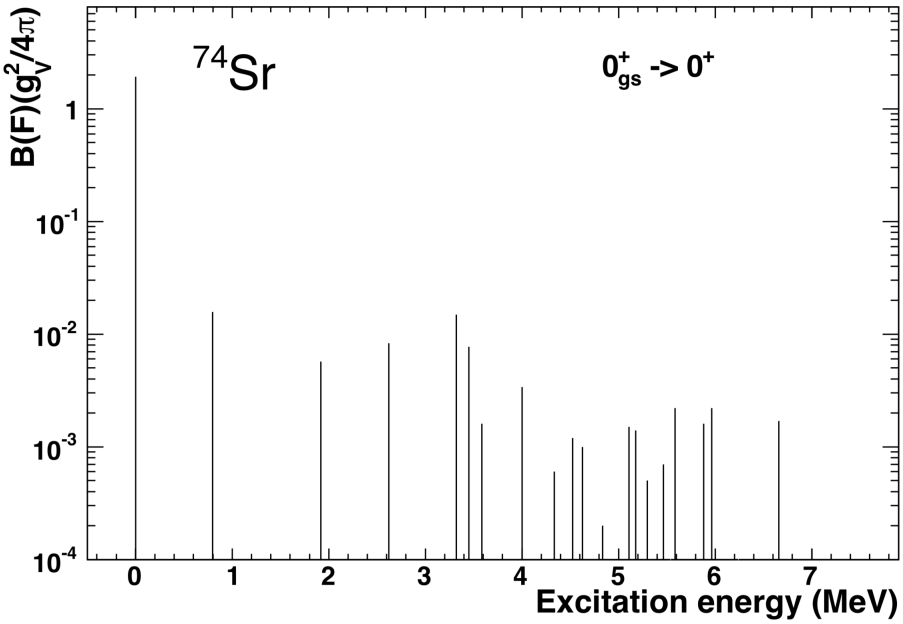

Figure 1. Fermi strength distribution for the decay of the ground state in ^{74}Sr to daughter state in ^{74}Rb.

The terrestrial half-life for the allowed transitions is given by:

$$\frac{1}{T_{1/2}} = \frac{1}{K}\sum_{E_f} f(Z, E_f)[B_{if}(F) + B_{if}(GT)] \tag{7}$$

where E_f denotes the energy of the final state, K is 6146 s and $f(Z, E_f)$ are the Fermi integrals.

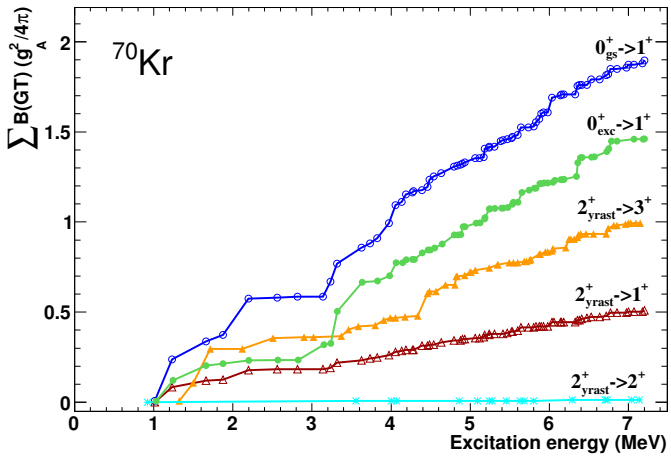

Figure 2. Gamow-Teller accumulated strengths(in units of $(g_A^2/4\pi)$ for the decay of the ground state, first excited 0^+, and yrast 2^+ state in ^{70}Kr to the daughter states in ^{70}Br obtained within the *complex* Excited Vampir model.

Theoretical Gamow-Teller accumulated strengths illustrated in Figure 2 for the decay of the low-lying 0^+ and 2^+ states in ^{70}Kr indicate stronger strength from the ground state

decay with respect to that from the first excited 0^+ state in ^{70}Kr, larger contributions from the decay of 2^+ states to daughter 3^+states than the ones to 1^+ states, and very weak transition strengths for the decay to daughter 2^+ states. Our predictions on GT strength distribution for the ground state decay are in agreement with preliminary data from recent measurements at RIKEN.

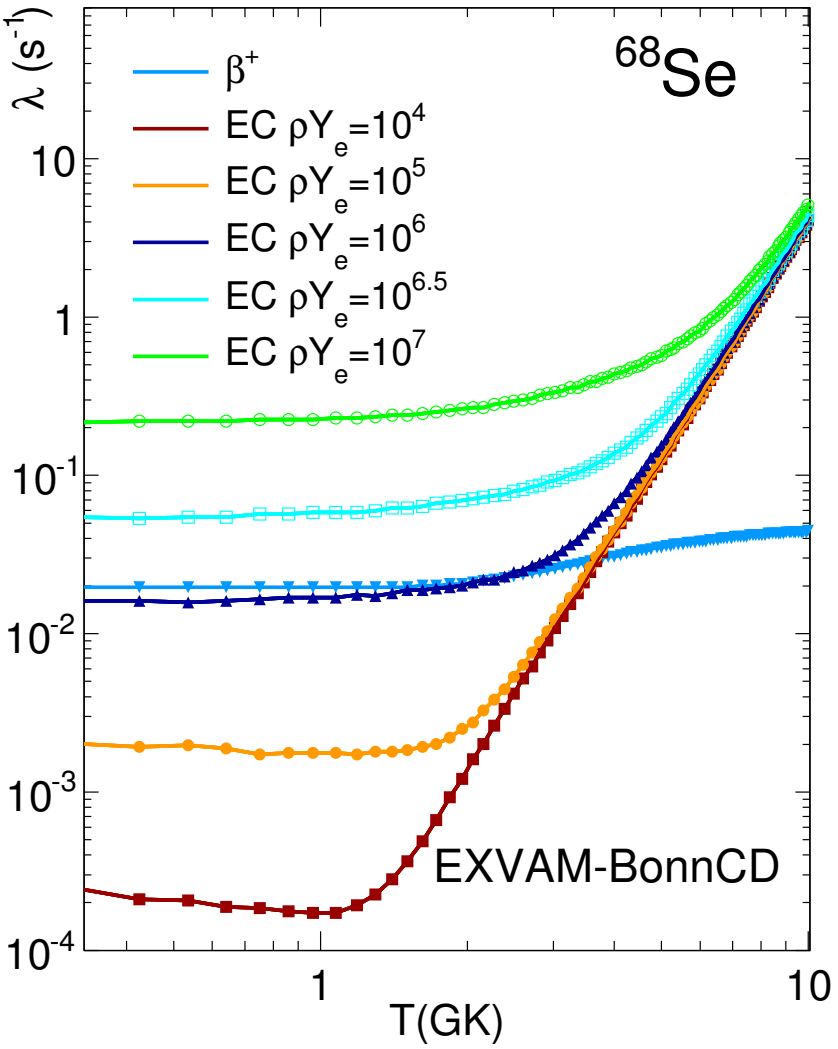

Figure 3. Decay rates (s^{-1}) for the ground state and yrast 2^+ state of ^{68}Se decomposed into the corresponding β^+ and electron capture components for selected densities $\rho Y_e(mol/cm^3)$ as a function of temperature (GK) obtained using the BonnCD potential.

Our scenario on the decay properties of ^{68}Se rp-process waiting point in the x-ray burst environment takes into account β^+ decay and continuum electron capture processes. Figure 3 illustrates the decay rates for the ground state and yrast 2+ state of ^{68}Se are decomposed into the corresponding β^+ and continuum electron capture components using Bonn CD potential. For the rp-process typical density $\rho Y_e = 106$ mol/cm^3, one can observe that for the results obtained using Bonn CD potential the electron capture overcomes the β^+ component only at temperatures larger than 2 GK.

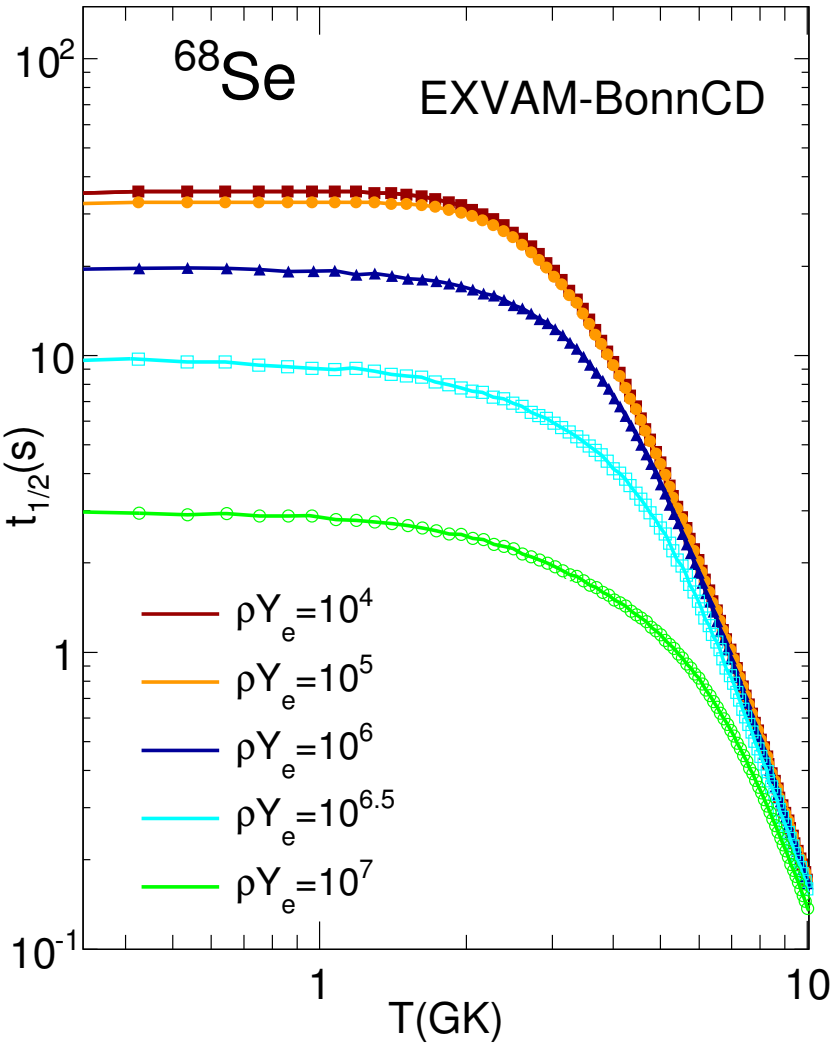

Figure 4. Half-lives (s) of ^{68}Se for selected densities ρY_e (mol/cm^3) as a function of temperature (GK) obtained using BonnCD potential.

The results on the half-lives of ^{68}Se for selected densities ρY_e as a function of temperature indicate a three times shorter half-life at T = 3GK and $\rho Y_e = 106 mol/cm^3$ with respect to the terrestrial value.

In the case of first-forbidden $0^- \rightarrow 0^+$ β decay there are two reduced matrix elements participating in this process:

$$\mathcal{M}_{FF1} = \left\langle \xi_f J_f^{\pi_f} || [\overrightarrow{\sigma} \cdot \overrightarrow{\nabla}]_0 || \xi_i J_i^{\pi_i} \right\rangle$$

$$= \sum_{ab} M_{FF1}(ab) \langle \xi_f J_f^{\pi_f} || [c_a^\dagger \tilde{c}_b]_0 || \xi_i J_i^{\pi_i} \rangle \tag{8}$$

$$M_{FF1}(pn) = \langle p || [\overrightarrow{\sigma} \cdot \overrightarrow{\nabla}]_0 || n \rangle \tag{9}$$

$$\mathcal{M}_{FF2} = \langle \xi_f J_f^{\pi_f} || [\overrightarrow{\sigma} \cdot \overrightarrow{r}]_0 || \xi_i J_i^{\pi_i} \rangle$$

$$= \sum_{ab} M_{FF2}(ab) \langle \xi_f J_f^{\pi_f} || [c_a^\dagger \tilde{c}_b]_0 || \xi_i J_i^{\pi_i} \rangle \tag{10}$$

$$M_{FF2}(pn) = \langle p || [\overrightarrow{\sigma} \cdot \overrightarrow{r}]_0 || n \rangle \tag{11}$$

Our aim was to find analytical solutions for the two reduced single-particle matrix elements M_{FF2} and M_{FF1} where both $\vec{\sigma} \cdot \vec{r}$ and $\vec{\sigma} \cdot \vec{\nabla}$ are forming a scalar product. The reduced single particle matrix elements using harmonic oscillator basis are:

$$\left\langle n_p l_p \frac{1}{2} j_p \left\| [\vec{\sigma} \cdot \vec{r}\,]_0 \right\| n_n l_n \frac{1}{2} j_n \right\rangle \tag{12}$$

$$\left\langle n_p l_p \frac{1}{2} j_p \left\| \left[\vec{\sigma} \cdot \vec{\nabla} \right]_0 \right\| n_n l_n \frac{1}{2} j_n \right\rangle \tag{13}$$

where n_i is the radial quantum number, l_i is the orbital angular momentum , j_i is the total angular momentum and 1/2 represents the spin, for both neutron and protons. The one-body operator consists of a product of two tensors acting on two different spaces coupled to a rank 0 tensor [8].

3 Results and future prospects

3.1 Results

During this internship I have written a code using Wolfram Mathematica that we have successfully used to evaluate numerically the reduced matrix element (11) for 10 different nuclei in mass regions from A=80 to A=210. We have found an analytical solution for $\int \vec{\sigma} \cdot \vec{r}$ that we compared with the numerical results and obtained relative differences of order 10^{-6} which enforce the validity of our analytical solution. We have also found our results to be in agreement with the literature [4,9,10].

3.2 Future prospects

An analytical solution for the second reduced matrix element, $\int \vec{\sigma} \cdot \vec{\nabla}$, is currently achieved and will be followed by the calculation of the four remaining matrix elements. Upon evaluating all single particle reduced matrix elements involved in first-forbidden β decay, the reduced one body transition density has to be calculated using the *complex* Excited Vampir wave functions in order to obtain the half-life and strength distributions. Realistic theoretical results obtained in the frame of the *complex* Excited Vampir model will be compared with the experimental data.Finally, reliable predictions on the weak interaction rates under astrophysical conditions could be obtained.

4 Acknowledgements

I would like to thank Prof. Dr. Alexandrina Petrovici for her guidance, perpetual patience and the opportunity to work in such a dynamic and exciting field, to Prof. Dr. Mihai Petrovici for his support and making this internship possible and the entire HPD team for an excellent work environment.

References

[1] Petrovici A, Schmid K W and Faessler A, 2011, *J.Phys.: Conf.Ser.* **312** 092051

[2] Petrovici A, 2012, *Phys.Rev. C* **85** 034337

[3] Petrovici A, Schmid K W and Faessler A, 2011, *Progr.Part.Nucl.Phys.* **66** 287

[4] Bohr A. and Mottelson B.R, 1969, *Nuclear Structure*,Vol.1, W.A. Benjamin, New York, Amsterdam

[5] Behrens H. and Buhring W., 1982, *Electron Radial Wave Functions and Nuclear Beta Decay*, Claredon Press, Oxford

[6] Weindenmuller H.A, 1961, *Rev.Mod.Phys* **33** 4

[7] Petrovici A, Andrei O., 2015, *Phys.Rev.* C**92** 064305

[8] Edmonds A.R., 1957, *Angular Momentum in Quantum Mechanics*, Princeton University Press, Princeton, New Jersey

[9] Civitarese O., Krmpotic F. and Rosso O.A., 1986, *Nuclear Physics:* **A453** 45-57

[10] Kenar I., Cevat S. and Kucukbursa A., 2005, *Mathematical and Computational Applications*, Vol.10, No.2, 179-184

List of projects

Students	**Project**	**Coordinators**
Iustin Ouatu, Liudas Karalius	TRD analysis	Dr. Alexandru Bercuci
Marius Tanase Manafu	Cosmic ray test of a high counting rate RPC prototype	Dr. Mariana Petris
Irina Maria Ionescu	CBM time-of-flight inner wall design	Dr. Laura Radulescu
Eusebiu Sutu	TRD FEE analysis	Dr. Ing. Catanescu Vasile
Amelia Lindner, Dana Avramescu	Features of p_T distributions and their $< p_T >$ as a function of centrality in Au+Au collisions at 7.7 GeV	Dr. Cristian Andrei, Dr. Andrei Herghelegiu
Adrian Sorin Mare	Weak interaction rates for exotic nuclei relevant in nuclear astrophysics	Prof. Dr. Alexandrina Petrovici

Lectures

Date	Hour	Speaker	Title of presentation
July 25	10:00	Dr. Alexandru Bercuci	Transition Radiation Detectors (TRD)
July 26	10:00	Prof. Dr. Alexandrina Petrovici	Exotic Nuclear Structure and Dynamics Relevant for Nuclear Astrophysics
July 27	14:00	Dr. Laura Radulescu	Mechanical Engineering Support for Nuclear Physics Experiments
July 31	11:00	Dr. Mariana Petris	Introduction in Resistive Plate Chambers for Time of Flight systems
August 3 August 4	11:00 09:00	Prof. Dr. Mihai Petrovici	Detection and Identification Methods in Nuclear and Particle Physics
August 7	11:00	Dr. Amalia Pop	Introduction in Heavy Ion Physics
August 8	10:00	Dr. Cristian Andrei, Dr. Andrei Herghelegiu	Introduction to Data Analysis using ALICE
August 9	10:00	Ing. Madalina Tarzila	Two–particle correlations in pp collisions at 7 TeV measured with ALICE at LHC

The HPD experience

Adrian Sorin Mare

University of Bucharest

During the Summer Student Program, I had the opportunity to gain an insight into the exciting field of nuclear structure and dynamics as well as to be involved into a cutting edge fundamental research. It was an inspiring experience that irreversibly shaped my goals and ambitions.

Amelia Lindner

University of Bucharest

For me, the Summer Student Program represented a step forward into the world of scientific research. I was able to get familiar with the exciting topic of high energy physics and it was a great opportunity for me to be able to work in such an environment, guided by top level scientists. After getting to know the insides of this world, I am proud to say that it gave a great start to a wonderful scientific journey.

Dana Avramescu

University of Bucharest

Being provided the unique opportunity to be a part of this student program, I spent my summer immersed into what now reveals itself as a truly remarkable experience. It was under the constant and careful guidance of scientists who deeply modeled my view on how top research should be conducted, that I was able to notice the patience and passion that one must possess in order to keep on being amazed by a physics that awaits to be discovered.

Eusebiu Sutu

University of Oxford

The summer program has given me the chance to work hands-on with the front-end electronics of the TRD detector and most important, to experience how the world-leading research is done. The weeks I spent here were interesting and helped me gain knowledge as well as meet interesting and passionate people.

Irina Maria Ionescu

Bucharest Technical University

This program was a glimpse into the immense knowledge and dedication of researchers in the field of nuclear physics and maybe a glimpse into the future.

Iustin Ouatu

University of Oxford

I had the chance to understand how research is conducted in a competitive physics laboratory and to learn about particle detectors, focusing on TRD. Now I also have knowledge about object oriented programming, basic concepts of data analysis and data acquisition systems.

Liudas Karalius

University of Birmingham

Putting yourself next to world–leading detector researchers sets up a unique environment to learn in. Though I gained understanding in a lot of topics, perhaps the most important of them – the process of research itself.

Marius Tanase Manafu

University of Birmingham

First time at this institute I came with hopes, doubts and excitement for the summer internship at the Hadronic Physics Department. Every day until the end of my work these slowly turned into a vision for what the institute and Hadronic Physics Department might look when the next generation works and learns with the more experienced generations into tapping the full potential found here.

Summer student party

Special thanks

We would like to offer our warmest regards and gratitude to the members of the Hadronic Physics Department for providing us the opportunity to work in such a remarkable environment, making it possible for us to get a glimpse at the unique landscape of scientific research, as seen through their eyes.

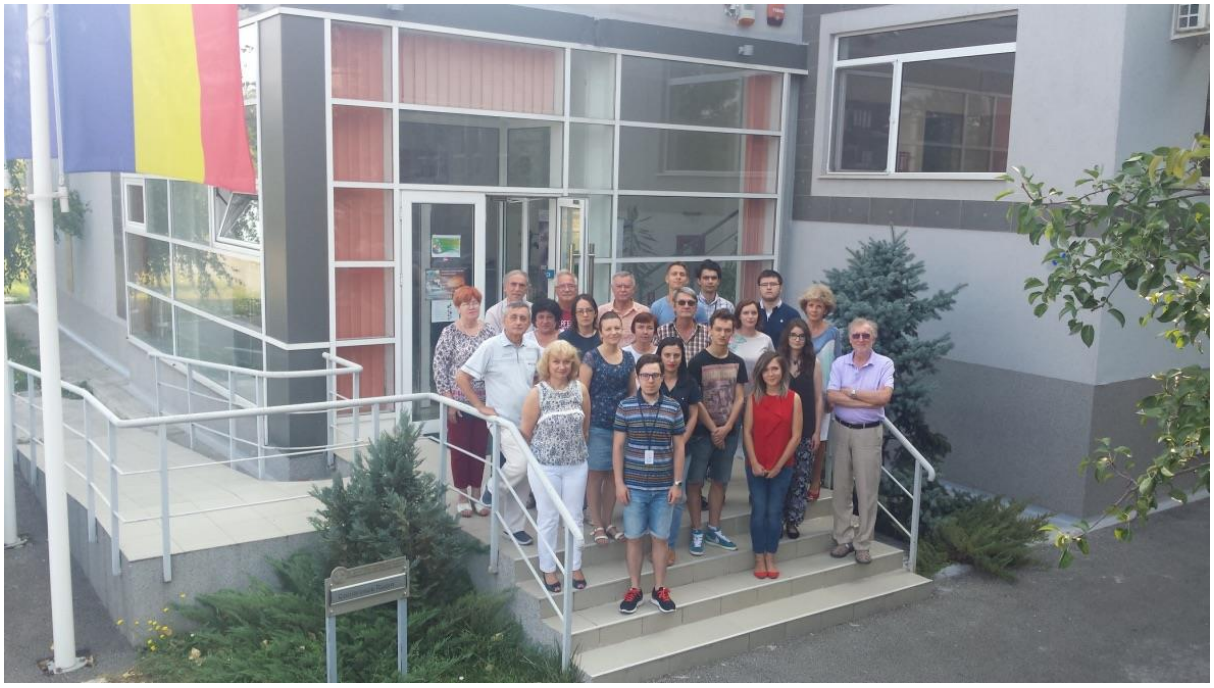

Horia Hulubei - National Institute for Physics and Nuclear Engineering (NIPNE), Bucharest
Hadronic Physics Department
Address Str. Atomistilor no.407, P.O.BOX MG-6, Bucharest - Magurele, ROMANIA
phone:0040-21-4042392 fax:0040-21-4574432
http://niham.nipne.ro